J. Fluid Mech. (2008), *vol.* 616, *pp.* 63–97. © 2008 Cambridge University Press
doi:10.1017/S0022112008003054 Printed in the United Kingdom

Dynamics of bubbles near a rigid surface subjected to a lithotripter shock wave. Part 2. Reflected shock intensifies non-spherical cavitation collapse

M. L. CALVISI[1]†, J. I. ILORETA[2] AND A. J. SZERI[1,2]‡

[1]Applied Science and Technology Graduate Group, University of California, Berkeley,
CA 94720-1708, USA

[2]Department of Mechanical Engineering, University of California, Berkeley, CA 94720-1740, USA

(Received 5 September 2006 and in revised form 3 May 2008)

In this paper we use the boundary integral method to model the non-spherical collapse of bubbles excited by lithotripter shock waves near a rigid boundary. The waves we consider are representative of those developed by shock wave lithotripsy or shock wave therapy devices, and the rigid boundaries we consider are representative of kidney stones and reflective bony tissue. This study differs from previous studies in that we account for the reflection of the incident wave and also the asymmetry of the collapse caused by the presence of the rigid surface. The presence of the boundary causes interference between reflected and incident waves. Quantities such as kinetic energy, Kelvin impulse and centroid translation are calculated in order to illuminate the physics of the collapse process. The main finding is that the dynamics of the bubble collapse depend strongly on the distance of the bubble relative to the wall when reflection is taken into account, but much less so when reflection is omitted from the model. The reflection enhances the expansion and subsequent collapse of bubbles located near the boundary owing to constructive interference between incident and reflected waves; however, further from the boundary, the dynamics of collapse are suppressed owing to destructive interference of these two waves. This result holds regardless of the initial radius of the bubble or its initial state at the time of impact with the lithotripter shock wave. Also, the work done by the lithotripter shock wave on the bubble is shown to predict strongly the maximum bubble volume regardless of the standoff distance and the presence or absence of reflection; furthermore, allowing for non-sphericity, these predictions match almost exactly those of a previously developed spherical model.

1. Introduction

Shock wave lithotripsy (SWL) is an established medical procedure for destroying kidney stones through the focusing of shock waves inside the body. These shock waves have an initial short compressive peak followed by a much longer rarefaction. This rarefaction can induce cavitation, which is believed to be an important contributor

---

† Present address: Department of Engineering Sciences and Applied Mathematics, Northwestern University, Evanston, IL 60208-3125, USA

‡ Author to whom correspondence should be addressed. aszeri@me.berkeley.edu

to stone comminution (Pishchalnikov 2003). A mechanism by which bubbles can damage nearby surfaces is through the generation of high-speed jets. For collapsing bubbles, the presence of a boundary creates an asymmetry in the flow field that causes non-spherical deformation and jetting towards the surface, as shown in both experiments (Crum 1979; Lindau & Lauterborn 2003; Sankin & Zhong 2006) and numerical simulations (Blake & Gibson 1987; Best & Kucera 1992). In addition, for bubbles stimulated by shock waves in an infinite fluid, the imposed pressure gradients can induce jetting in the direction of shock propagation. For example, Ohl & Ikink (2003) showed that microbubbles subject to travelling shocks collapse, then translate and form a thin high-speed jet along the direction of shock propagation. This jet can penetrate the opposite surface of the bubble and shed a small satellite bubble. Sankin *et al.* (2005) forced laser-generated bubbles with a lithotripter shock wave (LSW) at various stages during its ensuing oscillation, demonstrating that the bubble collapses non-spherically and forms a jet in each case.

In the case of SWL, both the presence of the rigid boundary and the propagating LSW may induce jetting of nearby bubbles. Jet formation from shock–bubble interaction has been linked to surface damage by Tomita & Shima (1986) who demonstrated damage pit formation in photoelastic materials owing to non-spherical bubble collapse. In addition, Kodama & Tomita (2000) showed the penetration of jets into gelatin owing to shock waves impinging on air bubbles attached to the surface. Other studies demonstrating the damage potential of shock–bubble interaction include those of Philipp *et al.* (1993) and Bourne & Field (1995). Thus, it follows that non-spherical bubble collapses are a likely contributor to stone damage in SWL.

Furthermore, the application of shock waves has been shown to enhance the damage potential of collapsing bubbles. Kodama & Tomita (2000) demonstrated that laser-generated cavitation bubbles near a gelatin surface did not generate significant liquid jets; conversely, air bubbles attached to the gelatin, which interacted with shock waves, created jets that subsequently penetrated the gelatin. Similarly, Sankin & Zhong (2006) showed that laser-generated bubbles near a silicone rubber membrane can produce deeper jet penetration when forced with a shock wave as compared to freely oscillating bubbles.

Various numerical studies on shock–bubble interaction are relevant to the present work. Ding & Gracewski (1996) modelled the impact of shock waves on gas bubbles using a finite-volume method whereas Klaseboer *et al.* (2006) conducted a similar study using the boundary integral method (BIM). Both of these works assumed the bubble to be far from any rigid boundaries and used a step-like model for the incident shock, which is not representative of shock wave profiles in lithotripsy. Other workers have modelled bubble collapses in the vicinity of a lithotripsy stone, but they did not account for either the reflection of the LSW from the stone surface or the non-spherical asymmetry of the bubble collapse (Zabolotskaya *et al.* 2004; Hamilton *et al.* 2005). As we demonstrate, both of these effects have a profound influence on the bubble dynamics and should be considered together in any study of stone comminution.

In Iloreta, Fung & Szeri (2008, hereinafter referred to as Part 1), the flow and pressure fields due to an LSW impinging and reflecting from an obstruction were modelled to replicate conditions typical of SWL. The properties of the obstruction were chosen to simulate the effect of a typical kidney stone on the surrounding fluid. In addition, the dynamics of spherical bubbles in the region near the stone were investigated. While the bubble is nearly spherical during expansion, the presence of a rigid boundary can cause severe asymmetry in the bubble shape during collapse, as discussed above. In Part 2, we consider non-spherical collapses and the associated energetics. The rigid boundary has two principal effects on the bubble dynamics: (i) it causes reflection of the incident LSW, which affects the work input into the bubble prior to collapse; and (ii) it creates an asymmetry in the flow field that causes the bubble to collapse non-spherically. Our goal here is to understand how these two mechanisms influence the bubble dynamics and energetics as a function of distance from the stone surface.

2. Methodology

2.1. *Physical assumptions*

Owing to the rapid collapse of bubbles in SWL, the flow is dominated by inertia, and viscous forces are relatively weak. For a typical collapse considered here, the bubble has a maximum radius $R_m \sim 1000\,\mu\text{m}$ with a collapse time $\tau_c \sim 100\,\mu\text{s}$. We may estimate a Reynolds number Re for the flow, assuming typical properties of water, using the velocity scale $U = R_m/\tau_c$ and the length scale $L = R_m$ as $Re = UL/\nu = (R_m^2/\tau_c)/\nu \approx 10^4$. In addition, assuming the fluid is initially quiescent, vorticity has little time to propagate from the surface of the bubble and the boundary-layer thickness δ_v is relatively thin. This can be quantified through $\delta_v/R_m \sim \sqrt{\nu\tau_c}/R_m = 1/\sqrt{Re} \approx 0.01$. We may therefore regard the fluid surrounding the bubble as irrotational, $\nabla \times \boldsymbol{v} = 0$, allowing us to represent the velocity $\boldsymbol{v}$ as the gradient of the scalar potential ϕ: $\boldsymbol{v} = \nabla\phi$.

Although the bubble dynamics are fast, the speed of sound in the liquid is much faster, allowing us to exploit the methods of Prosperetti & Lezzi (1986) who decomposed the fluid into two domains: an incompressible domain in the region near the bubble and a compressible region in the far field. We may assume the effects of the LSW are imposed from the far field onto the bubble, but that the behaviour of the fluid surrounding the bubble is essentially incompressible, i.e. $\nabla \cdot \boldsymbol{v} = 0$. The fluid mechanics can be then modelled using potential flow theory and reduced to solving the Laplace equation for ϕ,

$$\nabla^2\phi = 0. \tag{1}$$

This model holds well while the bubble wall velocity is much less than the speed of sound, but loses validity once this is no longer the case. For example, in some cases of shock-induced bubble collapse, jet velocities can approach the speed of sound of the fluid, as shown by Philipp *et al.* (1993) and Ohl & Ikink (2003), or even exceed it, as predicted by Ding & Gracewski (1996) and Klaseboer *et al.* (2006) and shown by Bourne & Field (1992). For many of the bubbles considered here, the jet velocity is well below the speed of sound, but can approach, or even exceed it, in some cases. In these latter situations, however, during the majority of the oscillation, the flow velocity is still well below the speed of sound, thus, potential theory is valid. The limitations of the potential flow assumption are discussed further along with the jet velocity in § 4.6.

2.2. *Numerical model*

In modelling the collapse of non-spherical bubbles near a rigid boundary, we use a numerical model based on the BIM (Taib 1985; Blake, Taib & Doherty 1986). This model is capable of modelling axisymmetric bubble collapses and is identical in every respect to that described in Calvisi *et al.* (2007) save that a rigid boundary of infinite extent is included through use of the method of images (Blake *et al.* 1986). To review briefly, the BIM is an efficient method of solving the Laplace equation, (1), for ϕ in the fluid surrounding the bubble. The efficacy lies in the need to mesh only the bubble surface, which can be reduced to a one-dimensional curve owing to the axisymmetry of the bubble geometry. The rigid boundary is modelled through the use of an image bubble of equal size and distance located on the opposite side of the boundary. Given the initial values of the potential on the bubble surface, the normal velocity at this surface can be determined through an integral solution of (1) (Blake *et al.* 1986). The bubble shape is then advanced using a kinematic boundary condition specifying that a point on the bubble surface convects with the local fluid velocity. The dimensionless potential $\widetilde{\phi}$ is updated at the next time step using the dynamic boundary condition

$$\frac{\mathrm{D}\widetilde{\phi}}{\mathrm{D}\widetilde{t}} = \frac{1}{2}|\nabla\widetilde{\phi}|^2 - \frac{p_b}{p_0} + \frac{2\kappa}{We} + \frac{p_\infty(z,t)}{p_0}, \tag{2}$$

where p_0 is the hydrostatic pressure, p_b the pressure inside the bubble (gas plus vapour), and $p_\infty(z,t)$ is the far-field pressure, which may vary along the direction of LSW propagation z, as well as with time t. In addition, because of the small size of the bubbles, surface tension is appreciable and is represented by the second to last term in (2), where κ is the dimensionless mean curvature of the bubble surface, and We is the Weber number, defined as $We \equiv R_m p_0/\sigma$, where σ is the surface tension. Equation (2) is derived from the Bernoulli equation for unsteady flow and incorporates all of the important physical processes into the model. The scales used to render (2) dimensionless are discussed in § 2.2.1.

Our BIM model uses a van der Waals equation of state for the bubble interior, owing to the intense nature of the collapses investigated, as described in Calvisi *et al.* (2007). The bubble interior is also assumed to consist of a uniform mixture of vapour and inert gas (argon). We include the effects of heat transfer across the bubble surface along with vapour transport (evaporation and condensation) by the method of Szeri *et al.* (2003). During the expansion phase of the bubble oscillation and the early stages of collapse, the bubble dynamics are slow relative to the processes of heat and mass transfer; therefore, it is assumed the bubble interior remains isothermal relative to the surrounding fluid, and that vapour can freely evaporate and condense at the bubble wall. We refer to this as the phase of 'slow' dynamics. In the latter stages of collapse, owing to the rapid bubble motion, heat and vapour do not have sufficient time to diffuse across the bubble interior. On this short time scale, the bubble is effectively adiabatic and vapour transport is negligible. This phase of the bubble oscillation is referred to as that of 'rapid' dynamics. The amount of water vapour at the beginning of the rapid stage is fixed, but can dissociate and undergo chemical reactions if the interior temperature exceeds 1000 K. These chemical reactions are mainly endothermic in nature and tend to lower the internal bubble temperature (Storey & Szeri 2000).

We are interested in measures of the fluid dynamics that may intuitively relate to damage at the surface of the kidney stone. Two such quantities are the kinetic energy and the Kelvin impulse, the latter of which can be regarded as a measure of the global fluid momentum at any instant of time. These quantities are calculated only for the fluid exterior to the bubble as they are negligible for the interior gas owing to its much smaller relative density. For a strictly spherical oscillation in an infinite fluid, the Kelvin impulse is identically zero, whereas kinetic energy is generally not;

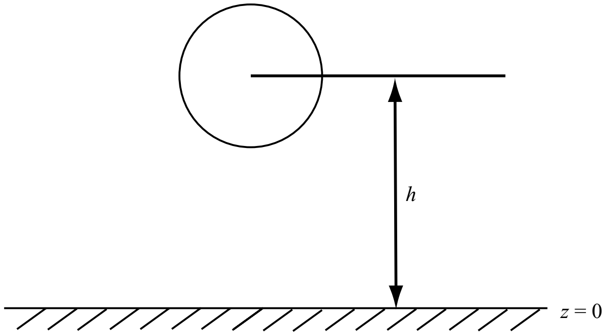

FIGURE 1. A schematic of the initial position of the bubble located a distance h from a rigid surface, which is positioned at $z = 0$. The positive z-direction is upwards.

but for a non-spherical collapse, both quantities are typically non-zero. Hence, they are independent quantities and, in addition, the Kelvin impulse provides a measure of the asymmetry of the bubble. While the Kelvin impulse $\boldsymbol{I}$ is a vector quantity, owing to the axisymmetry of the problem, only the component normal to the wall, I_z, is non-zero (see figure 1 for the geometry of the problem). Use of the BIM then allows for I_z and the kinetic energy E_k to be calculated in a straightforward manner as integrals over the surface area S of the bubble (Pearson, Blake & Otto 2004; Calvisi 2006) using the following formulae:

$$E_k = \frac{\rho}{2} \int_S \phi \frac{\partial \phi}{\partial n} \, \mathrm{d}S, \tag{3}$$

$$I_z = -\rho \, \boldsymbol{e}_z \cdot \int_S \phi \, \boldsymbol{n} \, \mathrm{d}S, \tag{4}$$

where ρ is the fluid density, $\partial \phi / \partial n$ is the normal velocity, $\boldsymbol{e}_z$ is a unit vector in the z-direction, and $\boldsymbol{n}$ is a surface normal vector defined as pointing into the bubble (away from the fluid), which leads to the minus sign in (4).

In order to model the influence of the LSW on the bubble, we input the pressure field data generated in Part 1 for the LSW–kidney stone interaction into our BIM model through $p_\infty(z, t)$ in (2) by the method of Calvisi *et al.* (2007). The wavelength of the incident LSW (compressive and tensile portions combined) is ~1 cm, which is much larger than the initial size of the bubble (~25 μm). Also, the time scale of the LSW (~10 μs) is much shorter than the expansion time of the bubble (~100 μs); hence, the incident and reflected waves pass long before the bubble reaches maximum volume. The majority of bubble translation occurs near the end of collapse when the jet forms and the bubble volume is shrinking rapidly and asymmetrically. Thus, while the LSW is acting on the bubble, it is essentially spherical, stationary and its size is close to its initial volume, much smaller than the wavelength of the LSW itself. Therefore, we neglect the spatial gradient of the pressure field and drive the bubble with the pressure calculated in Part 1 at the bubble's initial position. This is equivalent to assuming the pressure imposed by the LSW is spherically symmetric with respect to the bubble. We use only pressure data along the stone's axis of symmetry where the assumption of bubble axisymmetry is expected to hold. It is important to note that, in our model, non-spherical shape perturbations of the bubble are induced by the asymmetry in the flow field created by the nearby rigid boundary and not by the LSW itself. The effect of the axial spatial gradient of the LSW, however, will be explored in § 4.2 by incorporating it back into the model through $p_\infty(z, t)$ in (2). We also neglect the radial gradient in the pressure field because, during its interaction with the LSW, the bubble size (∼25 μm) is small compared to the radius of the stone (3.3 mm) assumed in Part 1.

In addition, we use data on the proximal side of the stone as this is expected to lead to the most intense collapses. This is supported by Pishchalnikov *et al.* (2003) who demonstrated through experiments that bubble clusters and subsequent damage are much greater on the proximal side of the stone than on the distal side. Furthermore, the deepest rarefaction, and probably the most intense collapses, occur along the axis of symmetry – where we assume the bubbles to be located – owing to constructive interference of the edge wave propagating radially inward from the edge of the cylindrical stone (see Part 1 for a discussion of this effect).

In essence, we are coupling together two different models and exploiting the best features of each in order to understand the physics of non-spherical bubble collapse due to interaction with an LSW near a substrate. The compressible Euler equations are solved in Part 1 to determine the pressure field in the vicinity of a kidney stone interacting with an LSW. We then input these data into the BIM model, which is very efficient at tracking moving interfaces, to simulate the collapse of non-spherical bubbles owing to the asymmetry imposed by the rigid surface. The pressure data developed in Part 1 account for density variations due to the incident LSW, but as the BIM is based on the assumption of an incompressible exterior liquid, it accounts only for pressure changes due to incompressible liquid dynamics associated with bubble motions. However, we do not expect this simplification to impact significantly on our results because, over the majority of the bubble oscillation, we can regard the near field of the fluid domain surrounding the bubble as incompressible owing to the relatively low flow velocity, as discussed in § 2.1. In certain cases, though, compressible effects will become appreciable during the latter stages of collapse when the flow velocity approaches the speed of sound. The rapid bubble motion will then lead to some energy loss through radiation of acoustic energy, but this will predominantly occur at jet impact – as shown in the experiments of Lindau & Lauterborn (2003) and Sankin *et al.* (2005) – and will therefore only affect the dynamics subsequent to this event. Some energy is also radiated from the bubble during the initial interaction between the LSW and the bubble; however, it is much smaller than that emitted at collapse (Ding & Gracewski 1996). As we limit our simulations to the singly connected phase of the oscillation (to be explained below), the small energy loss during this period will have little effect on our results. These arguments are supported by Klaseboer *et al.* (2007) who demonstrated the ability of the BIM to model accurately the dynamics of bubbles interacting with an LSW. In this work, an axisymmetric model based on the BIM, similar to the one used in this study, was compared to results of the experiments of Sankin *et al.* (2005) in which oscillating bubbles were subjected to an LSW. The numerical results from the BIM model match the experiments well, both qualitatively and quantitatively, despite being based on the assumption of an incompressible fluid. Based on this, we may conclude that the process of LSW–bubble interaction is dominated by inertia and that compressible effects are of minor importance. We defer further discussion of compressible effects to § 4.6.

There are some limitations to the use of our BIM model for this application. First, our BIM model is restricted to axisymmetric bubble shapes and cannot model three-dimensional effects as would be induced by nearby bubbles, irregular surfaces, or bubbles collapsing off the axis of symmetry. Secondly, the pressure data developed in

Scale	Symbol/form	Numerical value
Length	R_m	1168.83 μm
Pressure	p_0	101 325 Pa
Density	ρ	998.0 kg m^{-3}
Time	$R_m\sqrt{\rho/p_0}$	116.0 μs
Energy	$p_0 R_m^3$	161.8 μJ
Impulse	$R_m^3\sqrt{\rho\, p_0}$	16.06 μN s

TABLE 1. The relevant physical scales used in this study. Note that all scales of interest can be formed from the length, pressure, and density scales.

Part 1 assume a kidney stone of finite size, yet our BIM model assumes the boundary is of infinite extent. This assumption is made to allow the use of an image system to account for the stone surface (Blake *et al.* 1986), and is considered valid as long as the bubble is much smaller than the lateral extent of the proximal face of the stone, and the bubble is sufficiently close to the surface. Over the majority of the oscillation, the former assumption holds; however, near maximum volume, the effective diameter of the bubble can reach about one-third that of the stone. Also, at the larger standoff distances considered here, the bubble distance is approximately one diameter away. In these cases, the use of an infinite surface may cause the results to deviate from that of a finite surface. It is important to note that the effect of a finite surface is included in the pressure data used to force the bubble, for instance, incorporating the effect of the edge wave caused by the stone. More work must be done to understand the influence of a finite stone on the BIM calculation.

2.2.1. *Dimensionless variables*

We choose for the length scale $R_m = 1168.83\,\mu\text{m}$, where R_m is the approximate maximum radius of a bubble located about 1 mm away from the stone and that is driven by the rarefaction following the reflected compressive wave. This specific number is chosen as it divides evenly over the mesh used in Part 1 to generate the pressure field. We also use as scales the hydrostatic pressure, p_0, and the density of water under normal atmospheric conditions, ρ. These three scales – R_m, p_0 and ρ – allow us to form all other scales of relevance to this problem as shown in table 1. An important dimensionless parameter is the relative standoff distance, γ, which is the initial distance of the bubble centre from the rigid surface, h, divided by R_m

$$\gamma \equiv \frac{h}{R_m}. \tag{5}$$

A schematic of the initial position of the bubble relative to the wall is shown in figure 1.

2.3. *Forcing due to the LSW*

The presence of the wall has two principal effects on a bubble: first, it creates a reflected wave that alters the pressure field in the vicinity of the wall; second, it induces non-spherical collapse and jetting through the asymmetry in the domain occupied by the fluid. In order to isolate the effect of the reflection from that of the asymmetry, we use two separate pressure waveforms to excite the bubble: one that includes the combined effect of both the incident and reflected waves due to

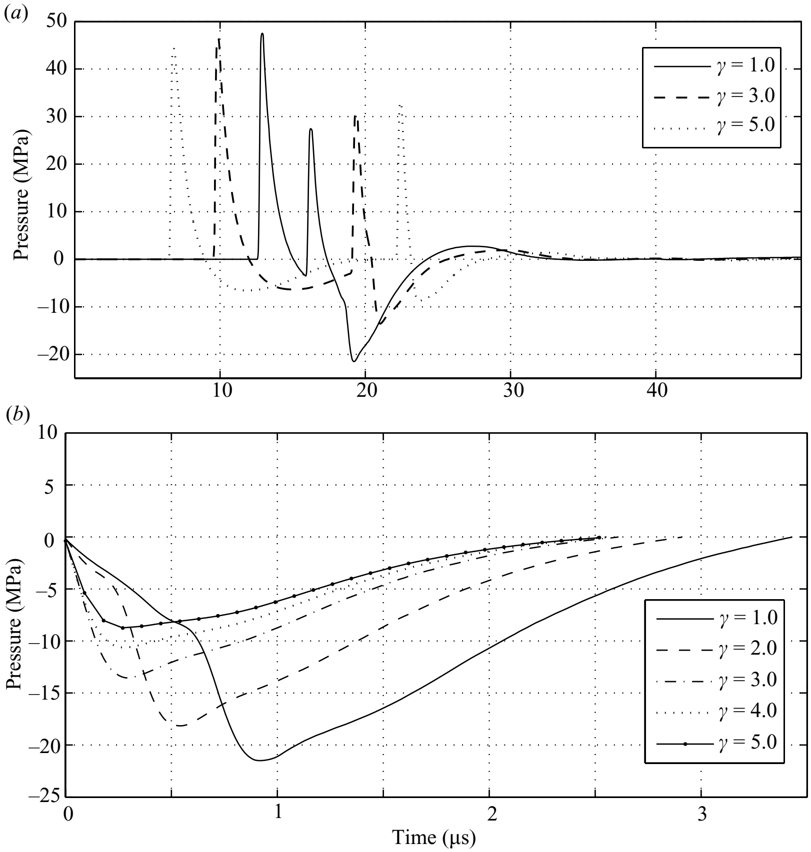

FIGURE 2. LSW pressure *vs.* time profiles along the axis of symmetry of the stone including reflection: (*a*) plots of pressure *vs.* time at the standoff distances, $\gamma = 1.0$, 3.0, 5.0; (*b*) plot of only the rarefaction portion of the LSW following the second compressive peak in (*a*) for $\gamma = 1.0$, 2.0, 3.0, 4.0, 5.0. The curves in (*b*) are shifted in time so as to start at $t = 0$. In general, the rarefaction depth steadily increases with decreasing γ, owing to constructive interference between the incident and reflected waves. These curves represent some of the pressure *vs.* time profiles used to force the bubble in the simulations of Case 1.

the LSW, and a second that includes only the effect of the incident LSW. In both cases, the bubble collapses are near a rigid boundary of infinite extent. The bubbles are driven by variations in the far-field pressure created by the passing LSW, as discussed in § 2.2. Plots of pressure *vs.* time at different standoff distances from the wall are shown in figures 2 and 3 for the case of reflection, and figure 4 for the case in which reflection is not considered. These pressure profiles are calculated numerically as discussed in Part 1 and represent typical LSWs propagating towards and focusing near a kidney stone. In all cases, the pressures shown are at points along the symmetry axis of the stone with no bubbles present. For the case of no reflection (figure 4), the LSW consists of a short sharp compressive peak followed by a rarefaction (negative pressure) that persists for a substantially longer time. The pressure then becomes positive again and oscillates about zero while steadily decaying in amplitude. The pressure waveforms for the case of reflection (figures 2 and 3) show that the reflected wave creates a secondary peak of reduced strength shortly after the first, with a rarefaction following. Note that the secondary rarefaction is much deeper

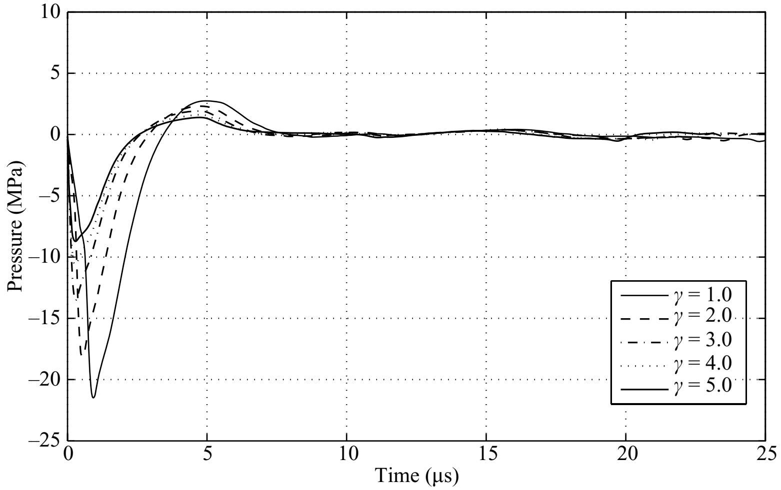

FIGURE 3. LSW pressure *vs.* time profiles along the axis of symmetry of the stone including reflection. These curves are extracted from figure 2(*a*) and include data from the start of the rarefaction following the second compressive peak to well past the end of the rarefaction. The curves shown are for the standoff distances, $\gamma = 1.0, 2.0, 3.0, 4.0, 5.0$ and are shifted in time so as to start at $t = 0$. These curves represent some of the pressure *vs.* time profiles used to force the bubble in the simulations of Case 2.

than the rarefaction for the case of no reflection. This enhanced rarefaction is due to constructive interference between the incident and reflected waves, as described in Part 1, and causes any bubbles present to expand to a larger maximum volume and collapse more intensely than if the wall were not present. In addition, there is much more variation in rarefaction depth and time span with γ when reflection is present (see figure 2*b*) as compared to when it is absent pressure inputs (see figure 4*b*).

To simulate the dynamics of bubbles subject to the pressure inputs shown in figures 2–4, we must consider the effect of each part of the LSW on the dynamics of the bubble. Referring to figure 2(*a*), we see there are five major components of the LSW with reflection. Proceeding in order of arrival time, the LSW can be decomposed into an incident compressive wave (ICW), incident tensile wave (ITW), reflected compressive wave (RCW), and a secondary tensile period (STP), followed finally by a rapidly decaying oscillatory portion we refer to as the ‘tail’. Note that the STP includes contributions from both the incident and reflected waves, whereas the ITW arises strictly from the incident wave. For the case without reflection, the LSW consists of only a leading ICW, followed by an ITW, and finally the tail (see figure 4*a*). We will use these terms to refer to specific portions of the LSW throughout the rest of the paper.

We argue that in our simulations, we may neglect the effect of the ICW altogether. In typical SWL applications, the temporal spacing between successive LSWs is ∼0.5–1.0 s (Pishchalnikov *et al.* 2006), whereas bubble oscillations dampen out after a few milliseconds at most (Matula *et al.* 2002). Therefore, bubbles will tend to be dissolving when encountering the steep pressure rise of the ICW and will collapse immediately and not contribute significantly to stone comminution owing to their small size. While experiments by Ohl & Ikink (2003) demonstrate that stationary bubbles subjected to an LSW in a free fluid can develop elongated high-speed jets in the direction of shock propagation, in our study, bubbles are located too far away for this mechanism to have

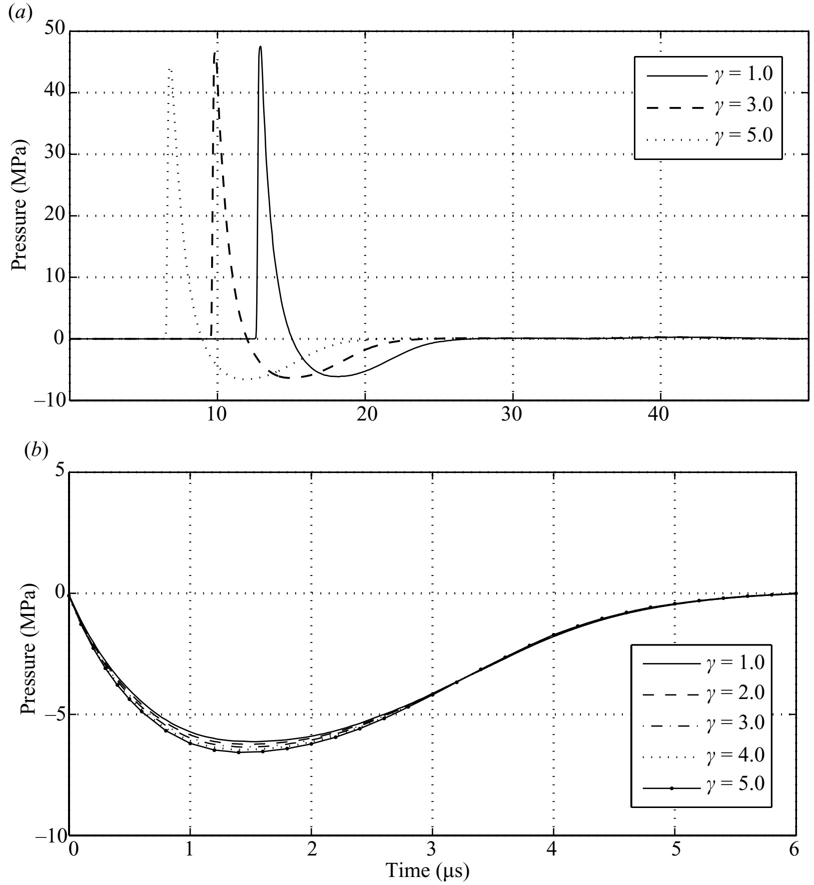

FIGURE 4. LSW pressure *vs.* time profiles along the axis of symmetry of the stone without reflection: (*a*) plots of pressure *vs.* time at the standoff distances, $\gamma = 1.0$, 3.0, 5.0; (*b*) plot of only the rarefaction portion following the incident compressive peak in (*a*) for $\gamma = 1.0$, 2.0, 3.0, 4.0, 5.0. The curves in (*b*) are shifted in time so as to start at $t = 0$. For the curves shown, the rarefaction depth increases slightly with increasing γ, owing to focusing of the LSW, and is greatest for $\gamma = 5.0$. These curves represent some of the pressure *vs.* time profiles used to force the bubble in the simulations of Case 3.

any impact on cavitation erosion. To be precise, Ohl & Ikink considered bubbles with initial radii in the range of 7–50 μm, similar to this study, and measured corresponding jet velocities and tip lengths upwards of 150 m s^{-1} and 150 μm, respectively. In the present work, we examine bubbles located ∼1–5 mm away from a rigid surface; therefore, jets from stationary bubbles of comparable size would contribute little, if anything, to surface damage. Furthermore, if we calculate the impulse imparted to an initially quiescent bubble by the Bjerknes force $\boldsymbol{F} = -(4\pi/3)R_0^3\nabla P(t)$ with an initial radius $R_0 = 25$ μm and using the pressure *vs.* time profile $P(t)$ in figure 2(*a*), we find that it is $\sim 10^{-10}$ N s. This impulse is negligible compared to the maximum Kelvin impulse generated by bubbles expanding and collapsing *after* passage of the ICW, which is of the order of $\sim 10^{-5}$ N s (to be discussed in § 3). This suggests that even for bubbles located very close to the kidney stone (∼1 mm), the ICW will be a secondary factor in inducing surface damage.

Case	Reflection from surface included?	Starting point for forcing	Portion of LSW used for forcing	Figure showing pressure waveforms used for forcing
1	Yes	Start of STP	STP only	Figure 2(*b*)
2	Yes	Start of STP	STP + ‘Tail’	Figure 3
3	No	Start of ITW	ITW only	Figure 4(*b*)

TABLE 2. The three cases of forcing used for simulations in § 3. The term ITW refers to the incident tensile wave, STP refers to the secondary tensile period, and ‘tail’ refers to the oscillatory portion of the LSW following the STP.

In contrast to the ICW, rarefaction during the ITW and STP intervals will tend to cause bubbles to expand to appreciable sizes and therefore collapse with much greater relative intensity (i.e. with larger values of kinetic energy and Kelvin impulse). As a bubble expands, it slows while increasing the potential energy of the bubble–liquid system. This potential energy is in turn converted to liquid kinetic energy during the subsequent collapse phase. It thus follows that, all else being equal, the larger the bubble expansion, the more violent the subsequent collapse and (we expect) the greater the ensuing cavitation erosion. For the case of no reflection, we then begin our simulations at the beginning of the ITW. For the case of reflection, we may consider starting the simulation at either the ITW or STP. Reference to figure 2(*a*) makes clear that the depth of the STP exceeds that of the ITW for the range $1.0 \leqslant \gamma \leqslant 5.0$; furthermore, for small values of γ, the time interval of the STP is longer than that of the ITW as well. This suggests that the STP is likely to be the main driver of the bubble dynamics, so for cases with reflection, we begin our simulations at the start of this period. The influence of the ITW and RCW on the results with reflection is investigated in § 4.4.

The next issue to clarify is when to end the pressure forcing. After passage of the STP, the ambient pressure becomes slightly positive, but eventually decays to zero after a few oscillations. Based on its greater magnitude, it is reasonable to assume that the STP will have a dominant effect on bubble growth and collapse as compared to the LSW tail. However, we test this assumption by performing simulations that include the tail portion of the LSW. In the interest of balancing completeness with economy of effort, we therefore consider three different cases of pressure forcing: Case 1 includes the STP for the reflected case; Case 2 includes both the STP and the tail for the reflected case; Case 3 includes only the ITW for the case of no reflection. In each case, the bubble is located near a rigid boundary of infinite extent. The reflection coefficient used for Cases 1 and 2 is 0.664. Case 3 can be interpreted as collapse near a stone with a reflection coefficient of zero, thus, all incident energy from the LSW is absorbed. Alternatively, Case 3 may be regarded as what is obtained when the reflection is (incorrectly) omitted. In all cases, we neglect reflections from the back of the stone and retransmission of shock energy into the liquid as this is likely to be negligible owing to the microheterogeneous nature of the stone (see Part 1 for a discussion of this). The pressure *vs.* time curves used to force the bubble in our simulations are shown in figure 2(*b*) for Case 1, figure 3 for Case 2, and figure 4(*b*) for Case 3. These three cases are summarized in table 2.

The trends for Cases 1–3 in the previous figures can be illuminated through calculating the work done by the LSW on the bubble. In Part 1, the work was calculated for the case of a spherical bubble. Here we extend this formulation to the case of a non-spherical bubble through the use of

$$W = \int_{V_1}^{V_2} p_\infty(z,t)\,\mathrm{d}V = \int_{t_1}^{t_2} p_\infty(z,t)\,\dot{V}(t)\,\mathrm{d}t, \tag{6}$$

where W is the work, $V(t)$ is the bubble volume at any instant of time, and the dot signifies a time derivative. The work done by the interior bubble pressure p_b is neglected in (6) as $p_\infty \gg p_b$ while the LSW acts on the bubble. Owing to the propagating LSW, the far-field pressure has a spatial gradient that varies along the z-direction. As argued previously, the size of the bubble during interaction with the LSW is much smaller than the wavelength of the LSW itself, thus, we can safely neglect the spatial variation in $p_\infty(z,t)$ in calculating W. In addition, the bubble's translation is negligible during passage of the LSW. Therefore, in (6) we use only the far-field pressure at the bubble's initial position h over the entire bubble. Note that a positive value of W corresponds to a decrease in kinetic energy and vice versa. For example, a negative pressure (rarefaction), $p_\infty(z,t) < 0$, causes volume expansion, $\dot{V} > 0$, leading to a negative value of W and an increase in the kinetic energy of the fluid, as we would expect. In Cases 1–3, the net work done by the LSW is always negative, although its magnitude may vary substantially, as will be discussed later. Also, as the far-field pressure is essentially zero after passage of the LSW, the only contribution to W is from the LSW itself.

2.4. *Initial conditions and fluid properties*

In § 2.3 it was argued that we should neglect the ICW, ITW and RCW of the reflected LSW and begin our simulations at the start of the STP. For cases in which reflection is neglected, simulations should begin at the start of the ITW. Determining initial conditions for the bubble at either of these points in the LSW cycle is another matter altogether. First, bubbles present in the urine space before LSW arrival, while most probably in equilibrium, may have a wide range of sizes. In addition, nucleation of additional bubbles may occur during passage of the LSW itself, either at the stone surface or in the surrounding fluid. Bubbles that encounter the steep pressure rise of the ICW will tend to collapse and may form jets, break up and/or reform during passage of the ITW. The negative pressure in the ITW will cause the bubbles to expand but, when we account for reflection, the compression of the RCW will suppress this tendency, further complicating the dynamics. Thus, the bubble size, shape and internal pressure may vary considerably at the beginning of the STP (or ITW for the case of no reflection) so that determining the initial conditions is not a trivial matter.

In Part 1, an initial radius of 4.5 μm was assumed; however, experiments by Ohl (2002) suggest that the initial radius after passage of the shock front of an LSW is ∼40 μm. For convenience, we assume the bubble has an initial radius of 25 μm and is in thermal and mechanical equilibrium with the surrounding fluid. The bubble is assumed to be initially spherical as it is expected that surface tension will round out the bubble quickly owing to any deformation caused by the leading part of the LSW. This assumption is reasonable, as we will show in § 4.4 that bubbles may survive past the RCW with little, if any, reduction in volume and with no apparent asphericity. Furthermore, our choice of R_0 is not critical as it was shown by Church (1989), Ohl (2002), and Iloreta *et al.* (2007) that the maximum volume of a spherical bubble interacting with an LSW is insensitive to initial size. This will be discussed further in

§ 4.1 where we show that for non-spherical bubbles, the maximum volume and other physical quantities of interest are also insensitive to initial radius. The state of the bubble (e.g. in equilibrium, expanding or collapsing) when acted upon by the LSW, however, does have some effect on our results and will be discussed in § 4.3.

In all cases we simulate a bubble collapsing in water with the following properties: hydrostatic pressure, $p_0 = 101\,325\,\mathrm{Pa}$; density, $\rho = 998.0\,\mathrm{kg\,m^{-3}}$; surface tension, $\sigma = 0.0728\,\mathrm{N\,m^{-1}}$; far-field temperature, $T_\infty = 298.0\,\mathrm{K}$; and speed of sound, $c_L = 1500\,\mathrm{m\,s^{-1}}$. The bubble interior is assumed to consist of water vapour plus argon (for convenience) with a ratio of specific heats of 1.667 and molecular weight of 39.95 g $\mathrm{mol^{-1}}$. Because a great quantity of vapour rapidly enters the expanding bubble, the vapour pressure greatly exceeds that due to the gas over almost the entire oscillation; therefore, the identity of the non-condensable gas (e.g. argon, air, nitrogen, etc.) is of little consequence. The initial vapour pressure is chosen to equal the saturated value at the far-field temperature T_∞.

2.5. *Non-spherical bubble dynamics*

A spherical bubble initially in thermal and mechanical equilibrium starts expanding upon interaction with the STP owing to the local negative pressure. This bubble continues expanding long after the LSW passes and eventually slows its expansion, achieves maximum volume, reverses direction, and collapses upon itself. During collapse, the bubble is drawn toward the rigid boundary as is well known. The presence of the wall causes the bubble to collapse non-spherically by inducing a jet to form on the distal side (relative to the rigid boundary) of the bubble (Blake *et al.* 1986; Lindau & Lauterborn 2003). This jet moves towards the rigid boundary along the axis of symmetry of the bubble and, if the collapse is sufficiently intense, penetrates through the bubble to the opposite side. If this occurs, the bubble undergoes a transition from a singly connected to a toroidal geometry. Calvisi *et al.* (2007) shows a typical bubble immediately before and after jet impact (also see figure 8).

The BIM model used in this study is capable of performing the conversion to a torus and continuing the simulation through this stage. The model uses the method of Best (1993), which removes a small section of the bubble between the bottom of the penetrating jet and the surface below and joins the two surfaces together (see Calvisi *et al.* 2007). Both the total energy and the Kelvin impulse are assumed to be conserved in the transition process. While it is understood that energy will be lost during jet impact owing to radiation of acoustic and/or shock waves and other dissipative processes, the assumption of energy conservation is used to simplify the analysis. Because of these dissipative mechanisms, and because the bubble starts re-expanding and the wall velocity slows almost immediately after jet impact, it is expected that both kinetic energy and Kelvin impulse of the liquid will achieve their maxima while the bubble is singly connected; hence, these calculations are not carried into the toroidal stage. Instead, we stop the simulation when the jet is within a specified (small) distance of the opposite bubble wall, using only quantities calculated during the singly connected phase.

In calculating kinetic energy and Kelvin impulse, we do so for the entire liquid domain and do not distinguish the contribution of the jet from the remainder of the liquid. Pearson *et al.* (2004) demonstrated that for the most vigourous collapses, approximately 30 % of the total kinetic energy and 50 % of the Kelvin impulse is manifested in the jet.

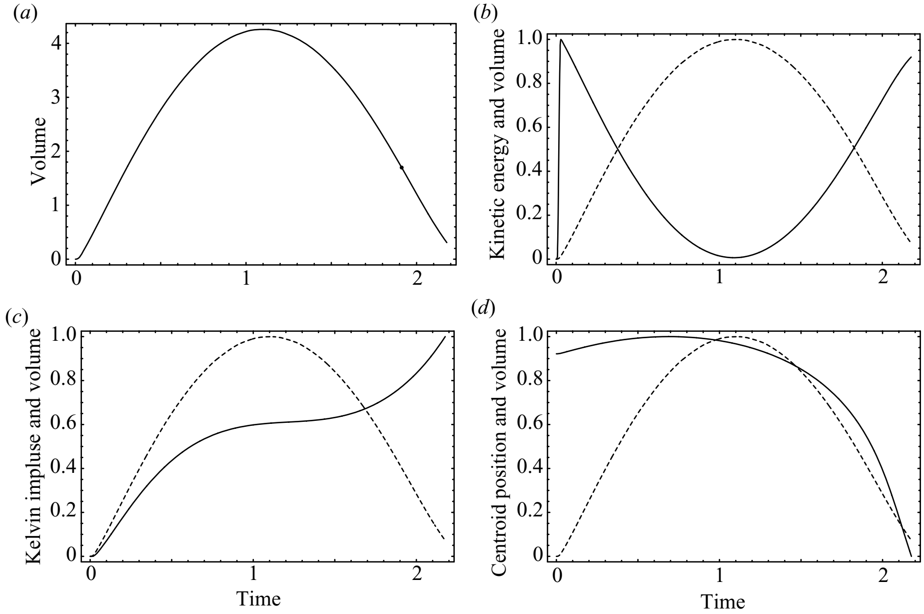

FIGURE 5. Plots of various physical quantities *vs.* time for Case 1 ($\gamma = 1.0$). The volume for (*a*) and the time in (*a*)–(*d*) are made dimensionless by the length and time scales, respectively, in table 1. The quantities in (*b*)–(*d*) are all normalized so that the maximum is unity. (*a*) Volume *vs.* time; (*b*) normalized kinetic energy (solid) and volume (dashed) *vs.* time; (*c*) normalized (absolute value of) Kelvin impulse (solid) and volume (dashed) *vs.* time; (*d*) normalized centroid position (solid) and volume (dashed) *vs.* time. The dot in (*a*) denotes the time of transition from slow to rapid thermodynamics as described in § 2.2. Plots of the same quantities *vs.* time for Case 3 are qualitatively similar to those of Case 1.

3. Results

In this section, we investigate the dynamics of LSW-induced bubble collapses as a function of distance from a nearby rigid boundary. Typical plots of volume, kinetic energy, Kelvin impulse and centroid position *vs.* time are shown for Case 1 in figure 5. Note that we plot the absolute value of the Kelvin impulse whereas it is actually negative in value because the bubble is drawn towards the rigid boundary in the negative z-direction (see figure 1). The work input of the STP the leading portion of the pressure input) causes volume expansion and a rapid increase in kinetic energy of the liquid. After the STP passes, the kinetic energy begins to decay to zero as expansion slows and the bubble approaches its maximum volume when the liquid becomes momentarily stationary. During collapse, the bubble wall accelerates inward and the kinetic energy again increases. For Cases 1 and 3, the total energy of the system after the passage of the STP is effectively conserved as the tail is not included in the forcing. Therefore, upon collapse, the kinetic energy rises to near the first peak (see figure 5*b*). The slight shortfall in kinetic energy upon collapse is due to conversion of some of the kinetic energy into thermal energy of the bubble contents (see Calvisi *et al.* 2007 for a discussion of this phenomenon). The bubble centroid translates only slightly during the early stages of the oscillation, as assumed earlier, but moves rapidly towards the rigid boundary during the latter stages as the kinetic energy and Kelvin impulse increase sharply. The plots in figure 5 are qualitatively similar for all

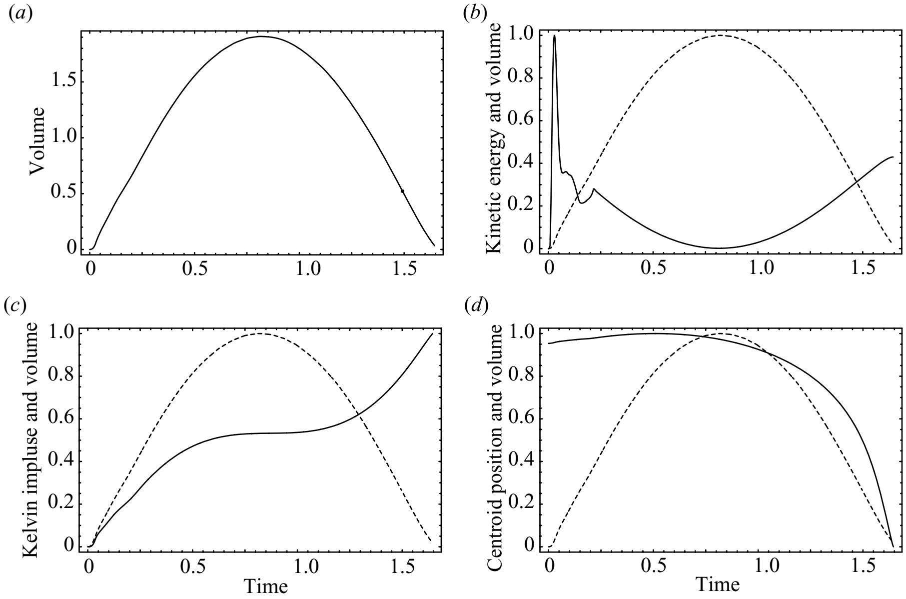

FIGURE 6. Plots of various physical quantities *vs.* time for Case 2 ($\gamma = 1.0$). The scales are the same as in figure 5. (*a*) Volume *vs.* time; (*b*) normalized kinetic energy (solid) and volume (dashed) *vs.* time; (*c*) normalized (absolute value of) Kelvin impulse (solid) and volume (dashed) *vs.* time; (*d*) normalized centroid position (solid) and volume (dashed) *vs.* time. The dot in (*a*) denotes the time of transition from slow to rapid thermodynamics as described in § 2.2.

simulations performed in Cases 1 and 3 where only the negative pressure of the STP is used to excite the bubble.

In Case 2, the inclusion of the tail portion of the LSW leads to a slightly different behaviour of the bubble. As in Cases 1 and 3, the kinetic energy rises rapidly owing to the STP, but the positive pressure from the tail portion inhibits further bubble growth, leading to a smaller maximum volume and substantially reduced kinetic energy upon collapse (see figure 6). Note that the action of the tail also causes a local dip in kinetic energy during the expansion phase of the bubble (see figure 6*b*).

3.1. *Influence of the rigid boundary on collapse*

The proximity of the rigid boundary has a profound effect on the bubble shape and the dynamics of the collapse (Pearson *et al.* 2004). In figure 7, we show a plot of the bubble volume *vs.* time for $\gamma = 0.7$–1.6 for Case 1. These plots are similar for Case 2 except that the maximum and minimum volumes are reduced; for Case 3, plots of volume versus time are qualitatively similar, but the maximum and minimum volumes vary little with γ. Note that as γ increases, the maximum volume of the bubble decreases, as does the minimum volume at jet impact. While the difference in maximum volume between the $\gamma = 0.7$ and $\gamma = 1.6$ cases is large, this represents a change of only about 30 % in the effective radius. Figure 8 shows the bubble shape at jet impact for Cases 1–3 for the same range of γ values as considered in figure 7. For $\gamma = 0.7$–1.0, there is significant flattening of the underside of the bubble near the wall for Cases 1 and 2, and the bubble is relatively large. As the standoff distance increases, say $\gamma \gtrsim 1.0$, a liquid layer exists between the bubble and wall, and the underside of the bubble at jet impact becomes rounder. In addition, the size of the

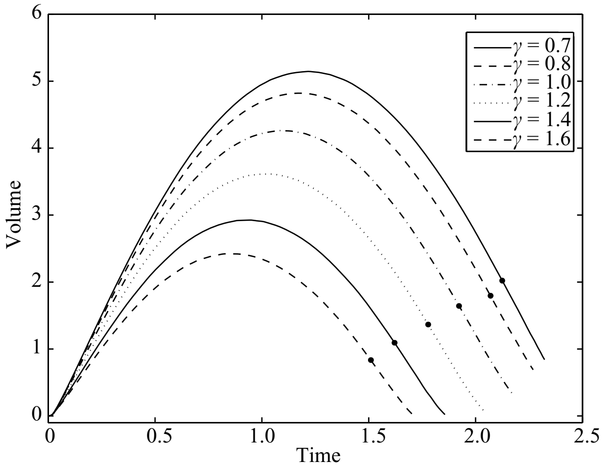

FIGURE 7. Overlay plots of dimensionless bubble volume *vs.* time for $\gamma = 0.7$, 0.8, 1.0, 1.2, 1.4 and 1.6 for Case 1. Note that as γ increases, the maximum volume of the bubble decreases and so does the minimum volume at jet impact. The dot represents the time at which the thermodynamics of the bubble interior switches from slow to rapid.

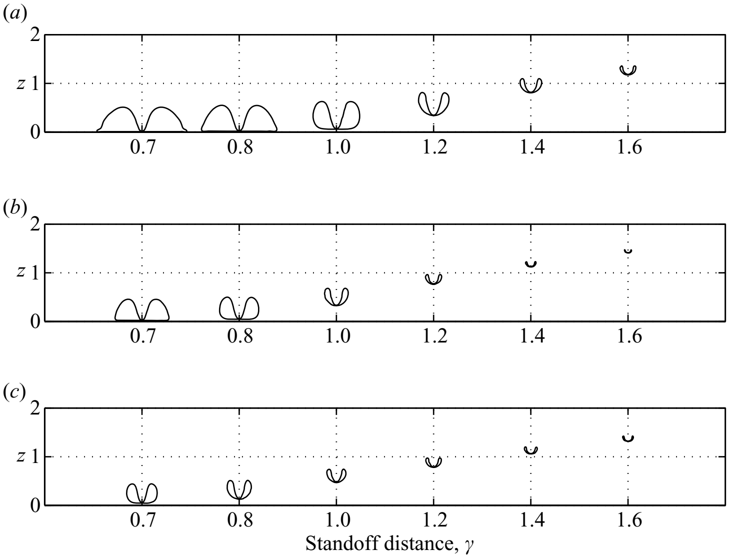

FIGURE 8. The bubble shape and distance from the wall at jet impact: (*a*) Case 1; (*b*) Case 2; and (*c*) Case 3. The same range of γ values is considered as in figure 7. The relative shapes and positions of the bubbles are shown to scale where the length in the z-direction is made dimensionless by the length scale in table 1.

bubble shrinks with γ, and the width of the jet relative to the bubble increases. These shapes compare very well to those shown by Tomita & Shima (1986) for bubbles generated by spark-discharge near a solid boundary, and also to those calculated by Pearson *et al.* (2004) for cavitation bubbles near a rigid surface. The shapes at jet impact for Case 3 are smaller and the underside of the bubble is rounder for $\gamma \leqslant 0.8$. The bubble size at jet impact (for all cases) continues to decrease as the standoff

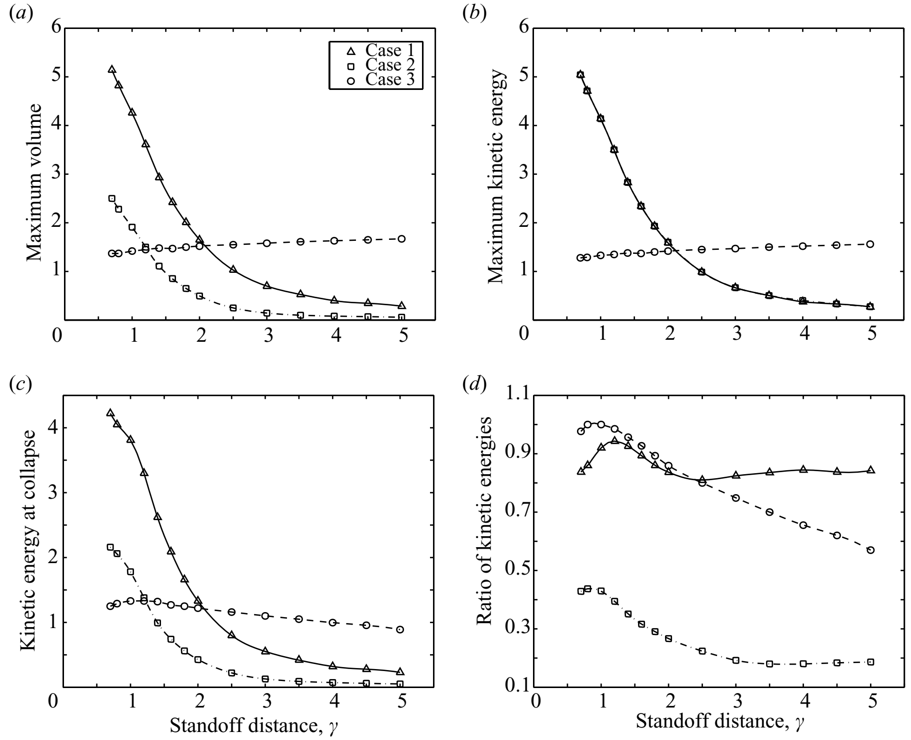

FIGURE 9. Plots of various dimensionless physical quantities *vs.* γ for Cases 1, 2, and 3. The markers represent the actual values from numerical simulations and the various curves interpolate these data points. The STP of the LSW is used as forcing input in all cases and the initial radius of the bubble is $R_o = 25\,\mu\text{m}$. The plots shown are the following: *a*) maximum volume *vs.* γ; *b*) maximum kinetic energy *vs.* γ (note that the curves for Cases 1 and 2 overlap); *c*) kinetic energy at collapse (jet impact) *vs.* γ; and *d*) ratio of kinetic energy at collapse to maximum kinetic energy *vs.* γ.

increases beyond $\gamma = 1.6$, but the shape remains similar to that for $\gamma = 1.6$. These shapes are not shown because of their small size.

Through calculation of the quantities of maximum volume, kinetic energy, Kelvin impulse, and centroid translation, we can gain a better understanding of the relationship between the dynamics of the bubble and its relative distance to the rigid boundary. Simulations were performed for the standoff distances in the range of $\gamma = 0.7$–5.0. The BIM model used here has difficulty modelling bubble collapses closer then $\gamma = 0.7$ owing to the evolution of sharp surface curvature which can lead to numerical errors. For all simulations considered here, the bubble starts off in thermal and mechanical equilibrium with the surrounding liquid and with an initial radius $R_0 = 25\,\mu\text{m}$. Aside from the type of imposed forcing (see table 2), the only parameter varied is the standoff distance γ. For each run, the maximum volume, maximum kinetic energy (which occurs during expansion), kinetic energy upon collapse, maximum Kelvin impulse, and net centroid translation are calculated. Note that all of these quantities are calculated while the bubble is singly connected. Plots of these quantities as a function of γ are shown in figures 9 and 10 for all cases.

The maximum volume *vs.* γ is plotted for Cases 1–3 in figure 9(*a*). The maximum volume of the bubble decreases rapidly and monotonically with increasing γ for

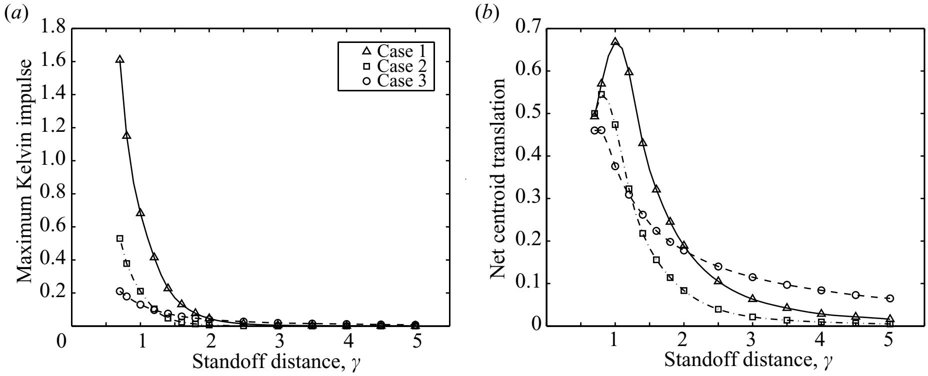

FIGURE 10. Plots of (*a*) maximum (absolute value of) Kelvin impulse *vs.* γ, and (*b*) net centroid translation of the bubble *vs.* γ, for Cases 1, 2, and 3. The markers represent the actual values from numerical simulations and the various curves interpolate these data points. All quantities are dimensionless. The input forcing and initial radius are the same as for figure 9.

Cases 1 and 2. The reduced maximum volume for Case 2 is due to the suppressing effect of the LSW tail after passage of the STP. For Case 3 the trend is different, showing that maximum volume is nearly constant, increasing only slightly with γ. The near constancy in maximum volume is due to the insensitivity of the ITW depth with respect to γ, as shown in figure 4(*b*). The results of Case 3 demonstrate that, for similar forcing, the proximity of the wall has virtually no effect on maximum volume, a similar result to that shown by Pearson *et al.* (2004). The strong dependence of the maximum volume on γ for Cases 1 and 2, therefore, is due to reflection of the LSW in the vicinity of the wall (cf. figures 2 and 3) rather than proximity of the rigid boundary.

3.2. *Bubble energetics*

Kinetic energy is calculated at two points during the oscillation of the bubble: (i) during expansion when it achieves a maximum, and (ii) at the moment of jet impact (collapse). These quantities are plotted *vs.* γ in figures 9(*b*) and 9(*c*), respectively, and display a dependence on γ similar to maximum volume. Note that the maximum kinetic energy of Case 1 is indistinguishable from Case 2 in figure 9(*b*) as the work input from the STP is the same in each case. The kinetic energy upon collapse, however, decreases by a factor of 2–3 when the LSW tail is included. This result mirrors the trend shown in figure 9(*a*) for maximum volume *vs.* γ: inclusion of the tail portion in the forcing inhibits the overall growth of the bubble and, consequently, the kinetic energy of the subsequent collapse. The results of Case 3 show that kinetic energy is approximately constant with respect to γ, similar to maximum volume.

Both maximum kinetic energy and kinetic energy of collapse increase monotonically as the bubble is positioned closer to the wall. This contrasts with the results of Pearson *et al.* (2004) who showed a peak in kinetic energy of the jet for $\gamma \approx 1.2$ when using an internal overpressure of fixed value to incite bubble expansion and collapse. Their results imply that jetting is most efficient when the bubble is located at a standoff of $\gamma \approx 1.2$. Our situation differs: the forcing of the bubble is not constant, but rather varies with standoff distance, and we calculate the kinetic energy of the entire liquid not just the jet. Calculating the ratio of the kinetic energy at collapse to the maximum kinetic energy, however, may yield a measure of jetting efficiency in our case. The kinetic energy ratio is plotted against γ in figure 9(*d*). For Case 1, there is a peak in the kinetic energy ratio at $\gamma = 1.2$ and for Case 2 it occurs around $\gamma \approx 1.0$, similar to the findings of Pearson *et al.* (2004). After the peak, the kinetic energy ratio for Case 1 is approximately constant with γ. For Case 3, ratio of the kinetic energies has a slight peak for $\gamma \approx 1.0$, but then drops steadily with increasing γ.

The Kelvin impulse yields insight into the non-sphericity of bubble collapse and the degree of jetting that cannot be quantified by kinetic energy, as discussed in § 2.2. For the collapses considered here, the (absolute value of) Kelvin impulse increases steadily with time, rising rapidly during the expansion, levelling off around the time of maximum volume, and then increasing rapidly again during the collapse phase (see figures 5*c* and 6*c*). Therefore, the maximum (absolute value of) Kelvin impulse always occurs at jet impact and these values are plotted in figure 10(*a*) for Cases 1–3. In each case, the Kelvin impulse decreases rapidly with increasing standoff distance demonstrating that the proximity of the rigid boundary has a very strong influence on the jetting process during collapse. In addition, the inclusion of the tail segment of the LSW (Case 2) reduces the maximum Kelvin impulse by a factor greater than two near the wall as compared to the case where only the STP is used to drive the bubble (Case 1). Case 3 has the lowest Kelvin impulse for low values of γ. As the bubble standoff is increase the collapse becomes approximately spherical and the Kelvin impulse approaches zero.

By comparing Cases 1 and 2 to Case 3 in figures 9(*a*–*c*) and 10(*a*), it is clear that reflection of the LSW enhances the maximum volume of the bubble and the kinetic energy and Kelvin impulse of the collapse in the vicinity of the wall. Away from the wall (i.e. for higher values of γ), the situation is reversed in that these quantities are greater when reflection is not included (Case 3), with the exception of the Kelvin impulse, which approaches zero in all cases as γ increases. The trend in the near region is due to constructive interference between the incident and reflected waves, which leads to a deeper rarefaction and enhanced bubble dynamics. Further from the surface, the incident and reflected waves interfere destructively, resulting in a suppression of bubble dynamics.

Our results for maximum volume, kinetic energy, and Kelvin impulse compare favourably to the experiments of Sankin & Zhong (2006) who used shock waves to impact laser-generated bubbles near a silicone rubber membrane and measured the subsequent penetration of the ensuing jet. The penetration depth reached a maximum for values of $\gamma \approx 0.7$ and declined steadily for higher γ, similar to the trends observed in figures 9(*a*–*c*) and 10(*a*).

3.3. *Bubble translation*

The asymmetry in the flow field created by a rigid surface causes a bubble collapsing nearby to translate toward it. In figure 10(*b*), we show the net translation of the bubble centroid (from the start of the simulation until the moment of jet impact) versus γ for all three cases considered here. For Cases 1 and 2, the centroid translation achieves a peak for $\gamma \approx 1.0$ and then steadily decreases for higher γ; in Case 3, centroid translation does not have a peak but declines after $\gamma = 0.8$. Essentially, the closer the bubble is to the wall, the more it is drawn toward it during collapse. If the bubble is too close, however, the wall apparently limits the centroid translation, giving rise to the peak around $\gamma \approx 1.0$ for Cases 1 and 2. For higher γ values, the translation of Case 3 exceeds that of both Cases 1 and 2, similar to the behaviour of maximum volume and kinetic energy.

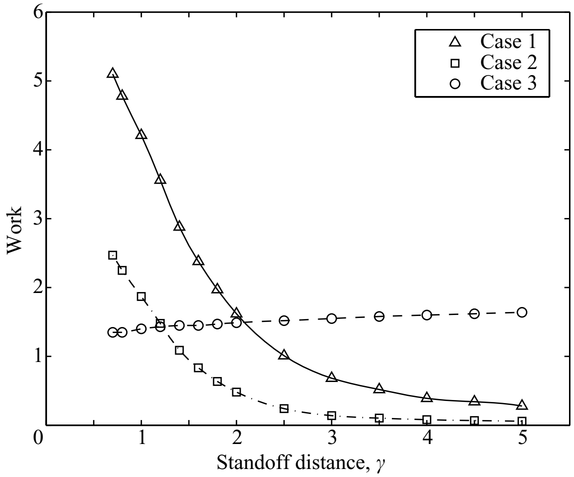

FIGURE 11. Plots of the dimensionless net work done by the LSW on the bubble *vs.* γ for Cases 1, 2 and 3. The markers represent the actual values from numerical simulations and the various curves interpolate these data points.

3.4. *The role of work done by the LSW*

The trends for Cases 1–3 in the previous figures can be illuminated through calculating the work done by the LSW on the bubble using (6). This quantity is negative for all the cases considered here, but, for convenience, we refer to the net work done by the LSW as a positive quantity hereinafter. The (absolute value of) work as a function of γ is shown in figure 11 for all three cases. The trends in work are similar to that of the maximum volume of the bubble: the work for Cases 1 and 2 decreases steadily with increasing γ, whereas the work for Case 3 is roughly constant. The net work done by the forcing in Case 2 is less than that of Case 1 for all γ owing to the compressive work done by the tail. However, it is clear that for lower values of γ, the work input for both Cases 1 and 2 exceeds that of Case 3, leading to more intense collapses and higher kinetic energy and Kelvin impulse in this regime, as shown in figures 9(*b*–*c*) and 10(*a*). Further away from the rigid boundary, the work input is greatest for Case 3. The trends in work input *vs.* γ for all cases follow directly from the effects of constructive and destructive interference of the incident and reflected waves as evidenced in the different plots of pressure *vs.* time shown in figures 2(*b*), 3 and 4(*b*). In the first two of these figures, the depth and time span of the STP decrease significantly with increasing γ leading to the large decrease in work input with respect to γ for Cases 1 and 2. In contrast, the pressure profile of the ITW in Case 3 has little dependence on γ, therefore, so does the work input shown in figure 11.

Now that we have a measure of work input, we can revisit the results shown in figures 9 and 10 and describe them in terms of an energy balance. The work input from the STP is the same in Cases 1 and 2 whereas Case 2 includes inhibitory work from the predominantly compressive tail segment of the LSW. The net work done by the STP acting on the bubble goes into increasing the kinetic energy of the liquid, which then is transferred to potential energy as the bubble expands. In Case 2, there is less potential energy stored in the liquid owing to the tail and subsequently less kinetic energy and Kelvin impulse during collapse. This energy balance helps to

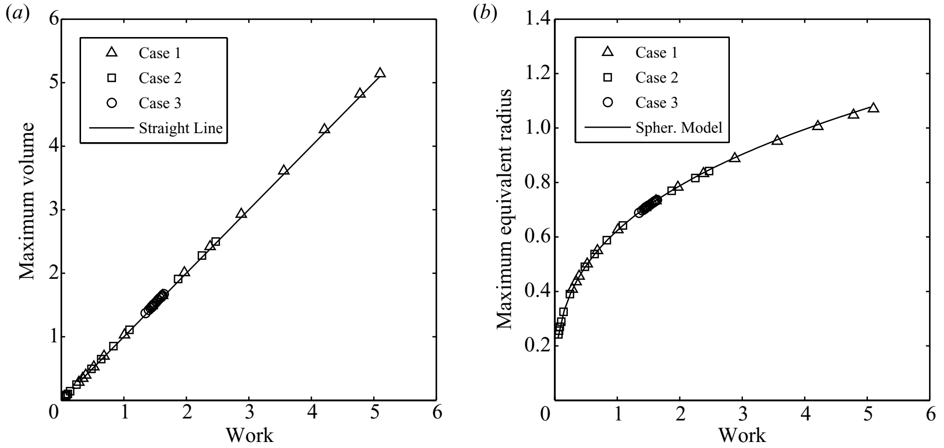

FIGURE 12. (*a*) Plot of maximum bubble volume *vs.* work done by the LSW on the bubble. Also plotted is a straight line of slope one passing through the origin of the graph. (*b*) Plot of the maximum equivalent bubble radius, $r_{e,max}$, *vs.* work done by the LSW on the bubble. The solid line is the relation between maximum radius and work by the spherical bubble model described in Iloreta *et al.* (2007), $r_{max} = 0.6238\, W^{0.337}$. The results of all simulations from Cases 1, 2 and 3 are shown. All quantities are dimensionless.

explain the results for Case 3 as well. As the work input is nearly the same at every standoff distance for Case 3, the maximum volume, maximum kinetic energy, and kinetic energy upon collapse are roughly constant with γ as shown in figures 9(*a*–*c*). Note that while maximum volume and maximum kinetic energy increase slightly with γ for Case 3 (see figures 9*a* and 9*b*), kinetic energy at collapse decreases slightly (see figure 9*c*). The first two quantities are directly proportional to the work input, which increases slightly with standoff distance for Case 3 owing to focusing of the LSW. The kinetic energy upon collapse, however, is mildly enhanced by the wall, which has less influence on the bubble the further away it is located. For all three cases, the proximity of the wall has a very dramatic influence on the Kelvin impulse as shown by its steep decline with increasing γ in figure 10(*a*).

The similarity between the plots of maximum volume and work *vs.* γ – as shown in figures 9(*a*) and 11 – is striking and suggests a relationship between the two quantities. The maximum volume versus the work input by the LSW on the bubble is plotted in figure 12(*a*). The results for all cases clearly lie on a single straight line. This is noteworthy given that, for a particular value of the work input, the standoff distance and pressure waveform used as forcing differ for each of Cases 1–3, yet the maximum volume is equal. The results in figure 12(*a*), therefore, strongly suggest that the net work done by the LSW uniquely determines maximum volume, regardless of the standoff distance of the bubble or the form of the LSW input.

We may compare the results in figure 12(*a*) for non-spherical bubbles to the model of Iloreta *et al.* (2007) for spherical bubbles. In this model, a power-law relation was derived between the work done on a spherical bubble and its maximum radius, r_{max}, using a Rayleigh–Plesset model incorporating gas diffusion, heat transfer, chemical reactions, surface tension and viscosity. Using the dimensionless scales in table 1, this relationship is given as

$$r_{max} = 0.6238\, W^{0.337}. \tag{7}$$

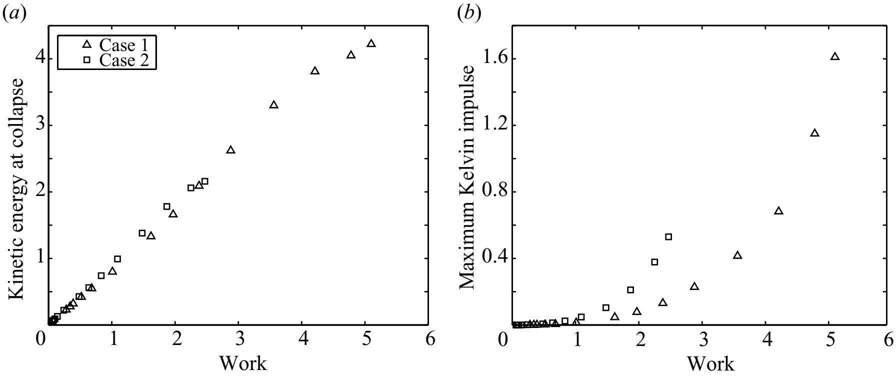

FIGURE 13. Plots of (*a*) kinetic energy at collapse (jet impact), and (*b*) maximum (absolute value of) Kelvin impulse vs. work done by the LSW on the bubble, for Cases 1 and 2 . Note that these results are only valid for bubbles collapsing with a high degree of asymmetry (i.e., in the near region) and should not be extrapolated beyond the range shown. All quantities are dimensionless.

Equation (7) was derived for bubbles with initial radius 4.5 μm, but is applicable to our study as it was shown in Church (1989) and Iloreta *et al.* (2007) that maximum radius (volume) is insensitive to initial radius. This finding is confirmed by our results and will be discussed in § 4.1. We compare our results here in Part 2 to the relation (7) by calculating an equivalent radius for the non-spherical bubble, $r_{e,max}$, in a straightforward manner from its maximum volume, V_{max}, using $r_{e,max} = (3V_{max}/4\pi)^{1/3}$. If we then plot $r_{e,max}$ versus the work input W calculated from (6) for each case, we see that the results match very closely the relationship given by (7), as shown in figure 12(*b*). This makes intuitive sense as the bubble is essentially spherical during its interaction with the LSW and subsequent expansion.

It would be ultimately helpful to link the work done by the LSW with quantities that are likely to correlate to damage of the underlying surface, such as kinetic energy and Kelvin impulse. The value in this approach is the replacement of the more complicated calculation of kinetic energy and Kelvin impulse for non-spherical bubbles with the relatively simple calculation of work, which can be reliably predicted through use of a spherical bubble model, as demonstrated above. For this reason we plot the kinetic energy at collapse and the maximum Kelvin impulse *vs.* the net work input in figures 13(*a*) and 13(*b*), respectively. We consider here only Cases 1 and 2 as these include reflection from the surface and thus are more physically realistic. Note that in figure 13(*a*) there is a strong one-to-one correlation between the work input and the kinetic energy at collapse, regardless of whether or not the tail is included in the forcing from the LSW. This trend does not hold for the Kelvin impulse as shown by the distinct curves for Case 1 and Case 2 in figure 13(*b*). These results suggest that kinetic energy at collapse could be reliably predicted through calculation of the net work input from the LSW but not necessarily the maximum Kelvin impulse. For determination of the Kelvin impulse at collapse, we must consider, for example, the standoff distance and the details of the forcing input. Note that the trends shown in figures 13(*a*) and 13(*b*) are only valid when the bubble is sufficiently close to the surface that its collapse is strongly non-spherical (i.e. in the near region). Far from the rigid boundary, the collapse will be approximately spherical yielding both a kinetic energy and a Kelvin impulse upon collapse that are nearly zero.

4. Discussion

The results presented thus far rest on several assumptions regarding the LSW–bubble interaction: (i) the results are insensitive to the initial radius of the bubble; (ii) the spatial gradient of the LSW can be neglected; (iii) the bubble is initially in equilibrium when acted upon by the STP; and (iv) the initial tensile wave (ITW) and reflected compressive wave (RCW) do not have a significant influence on the dynamics when reflection is considered. In this section, we investigate the sensitivity of our results to each of these assumptions. We restrict our analysis to Case 1 to account for reflection, which is more physically realistic; Case 2 is not considered as we have shown the results to be qualitatively similar to those of Case 1. Unless otherwise stated, all simulation conditions – forcing from the LSW, initial radius, etc. – are identical to those assumed for Case 1 in previous sections.

4.1. *Dependence on initial radius*

All previous results assume that the initial radius, R_0, of the bubble is 25 μm. To determine the sensitivity of the results to initial radius, R_0 was varied in the range of 15–50 μm and resulted in only a small change (10–20 %) in the maximum volume of the bubble and other quantities of interest (e.g. kinetic energy, Kelvin impulse). Note that a 20 % change in volume represents only about a 6 % change in radius for a spherical bubble. The choice of initial radius also did not qualitatively alter any of the trends of the data with respect to γ: enhancement occurs near the rigid boundary and declines steeply further away. The results are not shown here for the sake of brevity, but Calvisi (2006) shows plots of maximum volume, kinetic energy at collapse, and maximum Kelvin impulse for Case 1 for three different values of R_0: 15 μm, 25 μm (default value) and 50 μm.

The insensitivity of the results to initial radius has been shown in prior work, although for spherical bubbles. In Church (1989), the response of spherical bubbles in an infinite liquid subjected to excitation by a model LSW (similar to the one used here) was investigated using the Gilmore–Akulichev formulation of bubble dynamics. This model is similar to the Rayleigh–Plesset formulation, but includes compressible effects as well as gas diffusion. For initial radii in the range of 1–10 μm, Church (1989) showed there is very little variation in the maximum radius of the bubble for LSWs with compressive shocks greater than ∼20 MPa. In addition, for LSW profiles with an initial peak pressure greater than ∼30 MPa, similar to the LSW used here, other quantities such as the minimum radius, collapse time, radiated pressure, and the temperature inside the bubble demonstrate almost no dependence on R_0. The maximum bubble size is unaffected by the initial size as the amount of vapour diffusing into the bubble during expansion far exceeds the initial quantity of gas present (Matula *et al.* 2002). Ohl (2002) observed the explosive growth of cavitation bubbles in the wake of an LSW and further modelled them using a Gilmore model, which incorporates compressible effects. The experimental measurements matched very closely the modelling results, which demonstrated that the maximum radius of bubbles with initial radii in the range $0.1\,\mu\text{m} \leqslant R_0 \leqslant 100\,\mu\text{m}$ varies less than 10 %. Similarly, in Iloreta *et al.* (2007), a Rayleigh–Plesset model of spherical bubbles incorporating gas diffusion, heat transfer, chemical reactions, surface tension, and viscous effects was used to investigate the sensitivity of the bubble dynamics to initial radius. It was determined that the maximum radius of a spherical bubble subject to an LSW of a given strength is insensitive to R_0 in the range of 1–10 μm, and it is likely that other cavitation-related quantities are unaffected as well. However, maximum

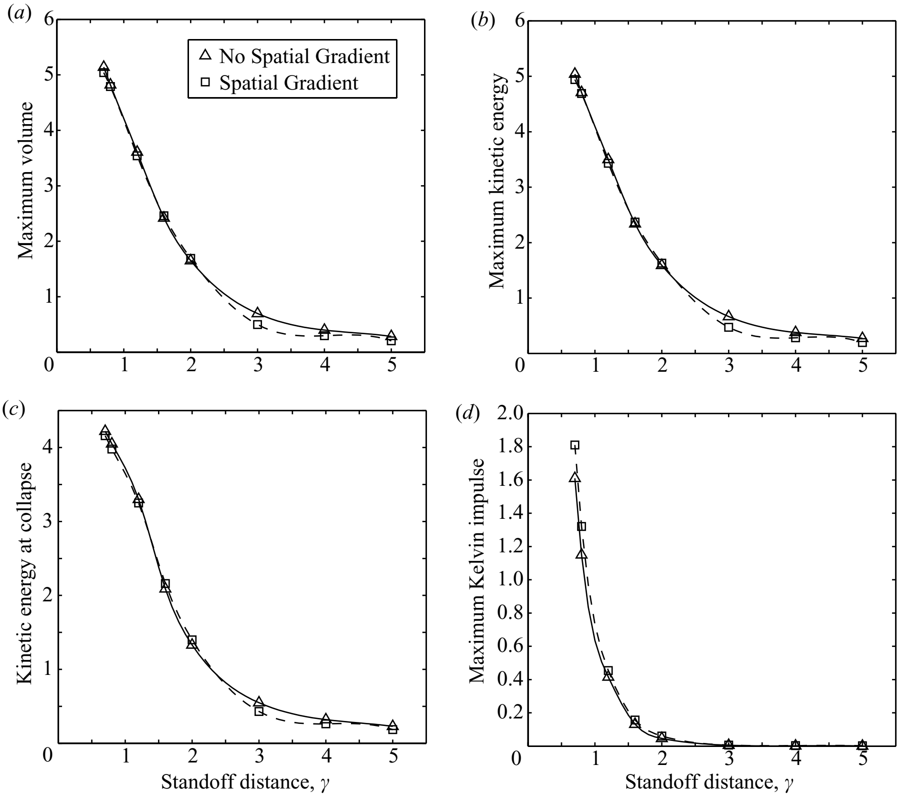

FIGURE 14. Plots of various dimensionless physical quantities comparing the results from the default Case 1 both with and without spatial gradient. The STP of the LSW is used as forcing input in both cases and the initial radius of the bubble is $R_o = 25\,\mu\text{m}$. The plots shown are the following: *a*) maximum volume *vs.* γ; *b*) maximum kinetic energy *vs.* γ; *c*) kinetic energy at collapse *vs.* γ; and *d*) maximum Kelvin impulse *vs.* γ.

radius depends strongly on the total work input by the LSW (similar to that shown in figure 12).

4.2. *Effect of spatial pressure gradient*

In § 2.2, we argued that owing to the small initial size of the bubble (25 μm) compared to the length of the LSW (∼1 cm), the spatial gradient of the pressure field along the axis of symmetry would not affect the bubble dynamics. Thus, we regarded the pressure imposed by the LSW (as calculated in Part 1) as uniform across the bubble, using only the pressure calculated at the bubble centroid to excite the bubble. Here we incorporate into the forcing the spatial gradient of the STP – the only portion of the LSW used to drive the bubble in Case 1 – and recalculate the quantities of maximum volume, kinetic energy, Kelvin impulse, and centroid translation. The results of these calculations are presented in figure 14 along with the results for the previous default Case 1 without a spatial gradient. It is clear that the spatial gradient has a negligible effect on the quantities of interest. Although the results for net centroid translation are not shown, the effect of the spatial gradient is minor, increasing it only slightly. It is also important to note that the spatial gradient does not cause any noticeable aspherical deformation during its interaction with the bubble. The STP passes very quickly during which the bubble has little time to expand and its shape remains effectively spherical. After passage of the STP, the bubble remains spherical during its expansion phase and begins to deform non-spherically only during the collapse. This demonstrates that the presence of the rigid boundary, and not the spatial gradient of the STP, is the main factor in inducing non-spherical collapse and jetting. While previous experimental studies of shock–bubble interaction in a free fluid (Ohl & Ikink 2003; Sankin *et al.* 2005) show that the spatial gradient causes jetting along the direction of shock propagation, in our case, the rigid boundary dominates this process, thereby justifying our previous use of a uniform driving pressure.

4.3. *Non-equilibrium conditions*

Thus far we have assumed that the bubble is initially in equilibrium (i.e. stationary and not oscillating) when acted upon by the STP. In actual SWL conditions, it is unlikely that bubbles present in the urine space surrounding the kidney stone will be in equilibrium after passage of the initial and reflected shocks. We therefore investigate the dynamics of bubbles that are initially oscillating and compare the results to our baseline results for equilibrium bubbles in Case 1. As the spatial gradient was shown to have a negligible effect in § 4.2, we disregard it here as was done previously throughout § 3. We may assume that after passage of the RCW, the bubble contents are compressed, causing the bubble to re-expand. The subsequent STP then impacts the bubble at some point during its rebound, e.g. during its expansion or collapse. To simulate such a non-equilibrium bubble, we set the initial internal pressure of a test bubble with $R_0 = 25\,\mu\text{m}$ to be one hundred times that of the ambient far-field pressure p_0. Because of the overpressure, the bubble in the absence of any external forcing will expand freely, achieving a maximum radius $R_{m,free}$. It is important to distinguish $R_{m,free}$ from R_m, which is the maximum radius of a bubble forced with an STP at $\gamma \approx 1$. In practice, $R_{m,free}$ is much smaller ($\sim$200 μm) than R_m ($\sim$1100 μm). Also, $R_{m,free}$ varies only slightly with respect to γ, whereas the maximum bubble volume due to forcing by the STP varies substantially with respect to γ (see figure 7). We then allow the STP to interact with the non-equilibrium bubble at various stages during its free oscillation and denote the radius of the bubble at the moment of impact as R_{hit}. Note that $R_{m,free}$ and R_{hit} are calculated separately for each γ and are based on the volume, $R = (3V/4\pi)^{1/3}$, which is meaningful as the free bubble remains almost perfectly spherical throughout its oscillation.

Four non-equilibrium conditions for bubble–STP interaction are examined assuming $R_0 = 25\,\mu\text{m}$ and an initial overpressure factor of 100, which leads to $R_{m,free} \approx 210\,\mu\text{m}$. These cases include the following: (i) $R_{hit} = R_0$ (or $R_{hit}/R_{m,free} = 0.12$) while momentarily stationary; (ii) $R_{hit}/R_{m,free} = 0.50$ during expansion; (iii) $R_{hit}/R_{m,free} = 1.00$ while momentarily stationary; and (iv) $R_{hit}/R_{m,free} = 0.50$ during collapse. A plot of radius versus time for the free bubble at $\gamma = 1.0$ is shown in figure 15 along with the various non-equilibrium cases considered. Note the small volume expansion relative to Case 1 (cf. figure 5*a*).

As the bubble may be compressed to a smaller size than 25 μm owing to the RCW, we also examine a case with $R_0 = 4.5\,\mu\text{m}$, as assumed in Part 1, and an appropriate overpressure so that it is not initially in equilibrium. To select the overpressure of this smaller bubble, we match its initial potential energy to that of the default equilibrium bubble with $R_0 = 25\,\mu\text{m}$. If we regard the potential energy as the product of the pressure and volume, then a 4.5 μm bubble with an overpressure factor of 170 has approximately the same potential energy as a 25 μm bubble in equilibrium. In

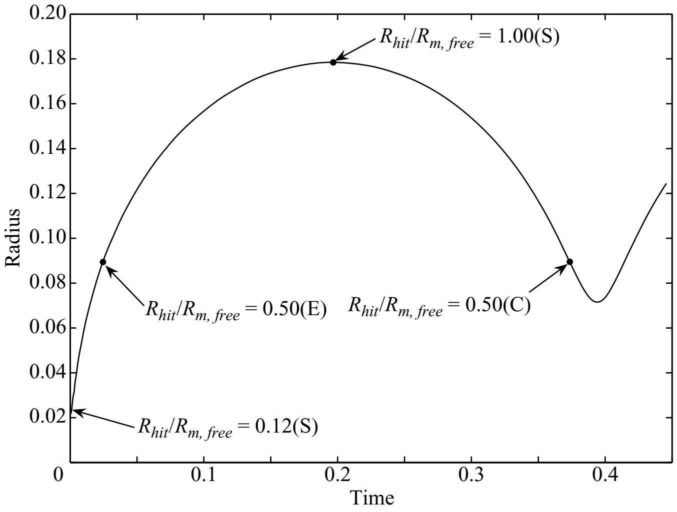

FIGURE 15. Plot of dimensionless (effective) radius *vs.* time for a non-equilibrium bubble oscillating near a rigid boundary ($\gamma = 1.0$, $R_0 = 25\,\mu\text{m}$) in the absence of forcing from an LSW, and with an initial overpressure factor of 100. In this case, $R_{m,free}$ is the maximum radius of the free oscillation and R_{hit} is the radius at the time of impact with the STP. The various points during the oscillation cycle at which the bubble is contacted with the STP are indicated with arrows, showing cases for expanding (E), stationary (S), and collapsing (C) bubbles.

our simulation, we allow the STP to interact with this 4.5 μm bubble while initially stationary.

Figure 16 shows plots of various quantities versus γ for the five non-equilibrium conditions considered – four with $R_0 = 25\,\mu\text{m}$ and initial overpressure factor of 100, and one with $R_0 = 4.5\,\mu\text{m}$ and an overpressure factor of 170. Also shown are the results for Case 1 ($R_0 = 25\,\mu\text{m}$, initially in equilibrium). The STP from Case 1 is used as the forcing in all the non-equilibrium simulations, the only difference being the state of the bubble at the time of the interaction. While the initial state of the bubble at the time of impact with the STP affects the magnitude of maximum volume, kinetic energy and Kelvin impulse, it does not affect the basic trends with respect to γ. In all cases, there is enhancement of maximum volume and collapse intensity near the rigid surface and a steep monotonic decrease of these quantities as the bubble standoff distance increases. A similar trend is observed for the net centroid translation (not shown) except that a peak occurs around $\gamma \approx 1$ similar to that seen in figure 10(*b*). In the four non-equilibrium cases with $R_0 = 25\,\mu\text{m}$, the collapse intensity is greater than that of the baseline equilibrium case, with the most intense collapses occurring for $R_{hit}/R_{m,free} = 1.00$(S), when the bubble is momentarily stationary at the time of STP-interaction. The results for the 4.5 μm bubble match almost exactly those for the default 25 μm bubble in equilibrium. This suggests that the strength of collapse may partially depend on the potential energy at the time of impact with the LSW, along with the work input by the LSW. This is supported by the fact that the potential energy of the non-equilibrium bubbles with $R_0 = 25\,\mu\text{m}$ exceeds that of an equilibrium bubble of the same size – owing to the higher initial overpressure – and the magnitudes of the associated scalar measures are correspondingly higher. Although this is an interesting observation, we do not explore this issue further here.

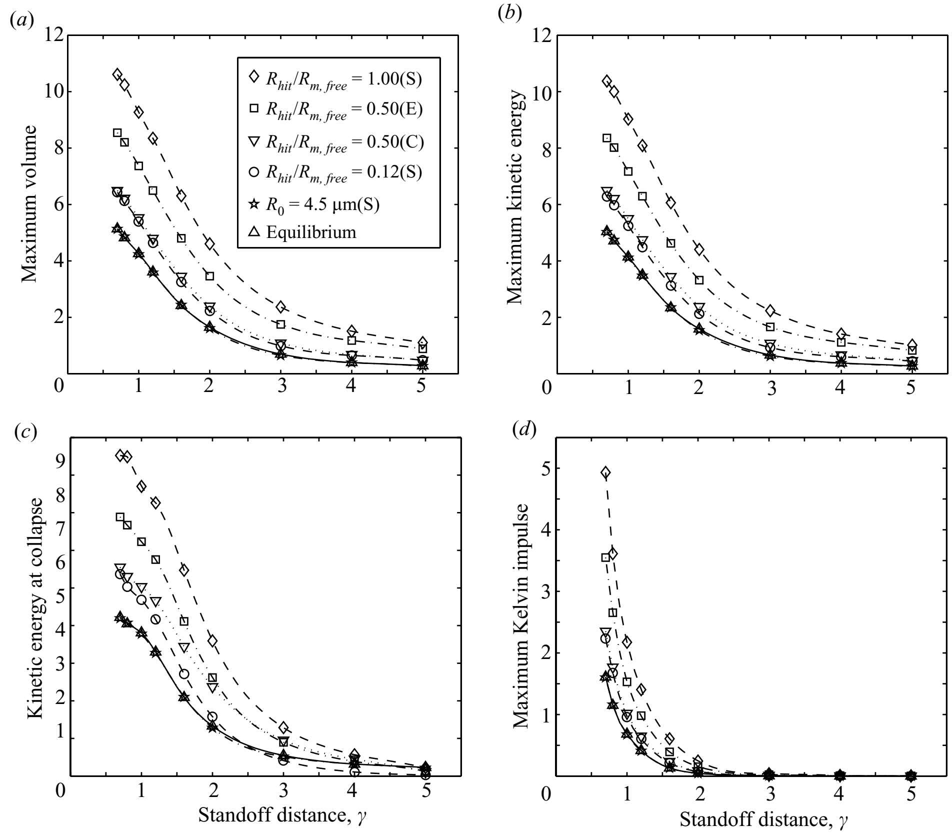

FIGURE 16. Plots of various dimensionless physical quantities comparing results from the default Case 1 at equilibrium ("Equilibrium") to those not initially at equilibrium. The STP is used for the forcing input in all cases. For the first four non-equilibrium cases, the initial radius is 25 μm, the overpressure factor is 100, and the bubble is contacted with the STP at various stages during its oscillation cycle, as depicted in figure 15. Results from a fifth case ("$R_0 = 4.5$ μm (S)") are shown for a bubble that is initially stationary with $R_0 = 4.5$ μm and an initial overpressure factor of 170. The results for this case match almost exactly those of the Equilibrium case. The plots show the following physical quantities: *a*) maximum volume *vs.* γ; *b*) maximum kinetic energy *vs.* γ; *c*) kinetic energy at collapse *vs.* γ; and *d*) maximum Kelvin impulse *vs.* γ.

4.4. *Influence of reflected compressive wave*

For the simulations performed in Cases 1–3, the forcing was initiated at the start of the STP. It was argued that this component of the LSW would be the main factor in determining collapse intensity as it would contribute most to bubble growth, and that the ITW and RCW would be of secondary importance. In this section, we test this assumption by including both the ITW and RCW in the driving pressure. We again neglect the spatial gradient of the LSW, as well as the influence of the ICW for the same reasons as given in § 2.3. We then compare the results based on including the ITW and RCW into the pressure input to those for our default Case 1 (which only uses the STP). Two sets of initial conditions are considered at the onset of the forcing by the ITW: (i) a bubble in equilibrium with $R_0 = 25$ μm; and (ii) an initially stationary bubble with $R_0 = 4.5$ μm and an overpressure factor of 170. Note that if we begin our simulations at the beginning of the RCW – thus neglecting the influence of the the ITW – then equilibrium bubbles collapse immediately owing to the compression, with negligible intensity. Therefore, we include the action of the ITW in order to set the bubble in outward motion before it encounters the RCW.

Values of maximum volume, kinetic energy and Kelvin impulse were calculated using a forcing input due to the combined effect of the ITW, RCW and STP, which we will refer to simply as the 'RCW' in the remainder of this subsection for simplicity. There are two distinct responses to the RCW, depending on the standoff distance. For small standoff distances ($\gamma \lesssim 1.5$), bubbles forced with the RCW collapse immediately with negligible intensity, regardless of the initial conditions. For $\gamma \gtrsim 2$, the scalar quantities of interest due to forcing with the RCW exceed those for Case 1. This behaviour is understood by considering the temporal spacing between the ICW and RCW. Near the stone, the RCW occurs quickly after passage of the ICW so that the time span of the intervening ITW is relatively short. This leads to only a modest increase in bubble size and inertia before the subsequent RCW rapidly collapses the bubble. For these bubbles, the simulation is halted when the distance between the upper and lower nodes along the axis of symmetry decreases below a specified small value (as discussed in § 2.5), and the simulation is not carried into the STP. The data for these values of γ are not shown as this would erroneously suggest that bubble collapses near the wall are not vigorous when, in fact, this is not the case. Bubbles crushed by the RCW are expected to re-form and re-expand during the subsequent rarefaction of the STP (see Lindau & Lauterborn 2003). These bubbles may then expand to an appreciable volume and collapse with significant intensity as shown in § 3. The proper initial conditions at the start of the STP in this case are difficult to ascertain; however, to a certain extent we have already addressed this issue in § 4.3 by exploring the sensitivity of the results to various initial conditions. To represent faithfully the cavitation potential in the region near the rigid boundary, instead of plotting the physical quantities due to forcing with the RCW, which are negligible, we show the values from Case 1 for $\gamma \leqslant 1.6$ (see figure 17). This is equivalent to assuming the bubble is in equilibrium with $R_0 = 25\,\mu\text{m}$ after passage of the RCW. Although this is unlikely, it has already been shown in § 4.1 that initial radius has little effect on the dynamics, and also in § 4.3 that the initial state of the bubble does not affect the overall trend of the data with respect to γ. In addition, the assumption of equilibrium after RCW passage in the near-field is consistent with the analysis in Part 1 for determining maximum bubble radius, thus allowing direct comparison. The consistency of our results with Part 1 will be discussed further below.

For larger standoff distances ($\gamma \gtrsim 1.5$), the ICW and RCW are separated further in time, allowing the ITW to act on the bubble for a longer period (see figure 2*a*). This increases the inertia of the fluid sufficiently so that the bubble survives the RCW. In fact, the action of the RCW tends to cause only a brief, minor reversal or slowing of the volume expansion at these larger values of γ. After passage of the RCW, the STP causes further volume expansion, which exceeds that due to the action of the STP alone. The larger volume expansion leads to an enhanced collapse intensity compared to Case 1. The physical quantities of interest due to forcing with the RCW are plotted in figure 17 for $\gamma \geqslant 1.6$.

In the case of forcing with the RCW, the results for $\gamma \geqslant 1.6$ are nearly identical for the two sets of initial conditions considered: $R_0 = 25\,\mu\text{m}$ in equilibrium and $R_0 = 4.5\,\mu\text{m}$ with a large overpressure. This mirrors the same findings in § 4.3 where forcing was due to the STP only. Thus, it appears that in addition to the work input by the LSW, the potential energy may be a strong predictor of the dynamics of the collapse process.

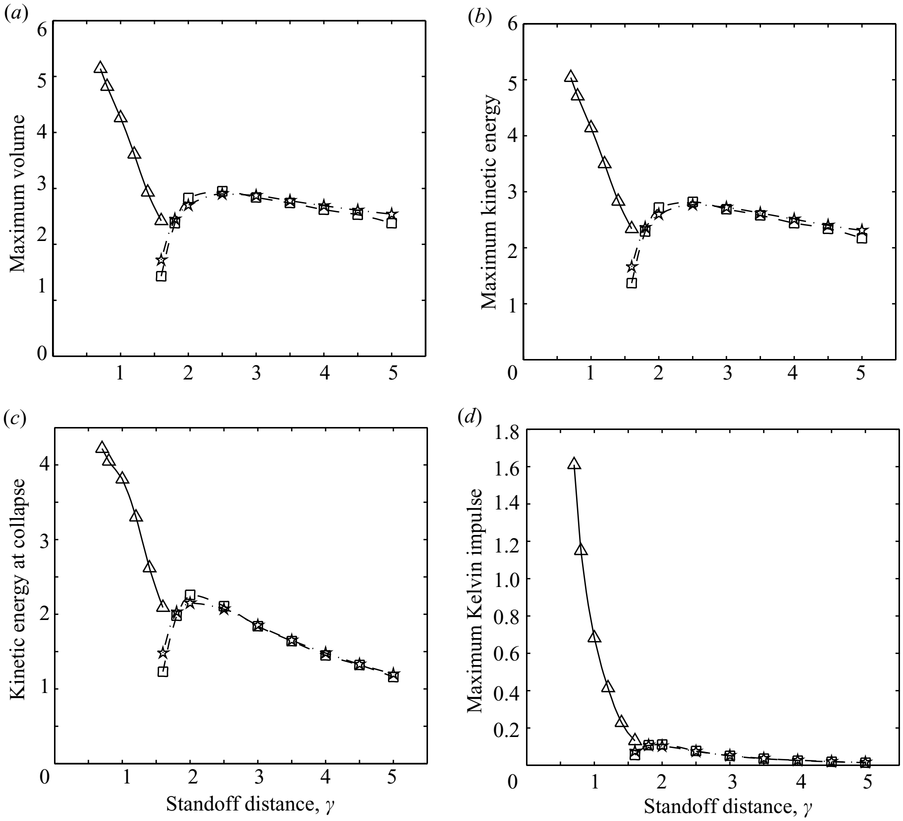

FIGURE 17. Plots of various dimensionless physical quantities showing results from △, the default Case 1 (forcing with the STP only) in the region $\gamma \leqslant 1.6$, and the results of two other cases forced with the combined effect of the ITW, RCW and the STP for $\gamma \geqslant 1.6$. The two latter cases include □, a bubble with $R_o = 25\,\mu\text{m}$ in equilibrium, and ⋆, a stationary bubble with $R_o = 4.5\,\mu\text{m}$ and an initial overpressure factor of 170. The spatial gradient of the LSW is neglected in all cases. The plots show the following physical quantities: (*a*) maximum volume *vs.* γ; (*b*) maximum kinetic energy *vs.* γ; (*c*) kinetic energy at collapse *vs.* γ; and (*d*) maximum Kelvin impulse *vs.* γ.

The data shown in figure 17 represents a composite due to two different types of forcing: the STP alone is used in the near region (Case 1), and the sequence consisting of the ITW, RCW and STP is used further away. The quantities of interest decline sharply with increasing distance from $\gamma = 0.7$ and reach a local minimum at $\gamma \approx 1.6$. Beyond this distance, the values increase, achieve a local maximum at $\gamma \approx 2.0$, and then decline slightly with increasing γ. The overall trends in figure 17 are very similar to those shown in Part 1 for the calculation of the maximum radius of *spherical* bubbles with respect to standoff distance. In the analysis of Part 1, forcing was initiated at the start of the STP for bubbles near the kidney stone, but at the start of the ITW for bubbles further away, similar to the representation in figure 17 for non-spherical bubbles. Consequently, the Part 1 results are very similar to those shown in figure 17, and demonstrate a maximum bubble radius that declines steadily with increasing distance and a local minimum around 2 mm, corresponding to $\gamma = 1.7$ here. The close agreement between the spherical model in Part 1 and the results for non-spherical bubbles presented here, further validates the use of (7) in predicting maximum volume (or radius) for a given work input.

One discrepancy between the results of Part 1 and those presented in figure 17 is the behaviour in the far field; for the former, maximum volume (or radius) levels off to a constant value, and for the latter, maximum volume decreases slightly but steadily with respect to standoff distance. This discrepancy can be explained through the action of the tail portion of the LSW, which is included in Part 1 but not for the results presented here. As the tail section is predominantly compressive, and is stronger near the wall (see figure 3), it is likely that it would flatten out the local maximum around $\gamma \approx 2.0$ shown in figure 17. This would then yield a behaviour in the far field similar to that shown in Part 1. Therefore, the relationship between the maximum volume of non-spherical bubbles and standoff distance is consistent with the purely spherical model in Part 1 even when the RCW is included.

The magnitudes of the physical quantities presented in figure 17 for $\gamma \geqslant 1.6$ are larger than those shown in figures 9(*a–c*) and 10(*a*). This difference arises from the initial conditions at the beginning of the STP. For the Case 1 study, the bubble is initially in equilibrium whereas the results presented in this section for $\gamma \geqslant 1.6$ are due to bubbles that are already expanding at the onset of the STP, because of the influence of the ITW. As was shown in § 4.3, bubbles in expansion at the start of the STP expand to larger volumes and collapse with greater intensity compared to those initially in equilibrium (see figure 16). Hence, figure 17 is consistent with previous results and indicates that the quantitative behaviour depends on initial conditions. However, the main effect of reflection from the wall – enhancing cavitation collapse in the near region and reducing it further away – is unaltered by the initial conditions of the bubble.

A few further observations are worthy of comment regarding inclusion of the ITI and RCW into the forcing input. First, for $\gamma \lesssim 1.5$ and spatial gradient neglected, the bubble collapses suddenly and the shape remains spherical as there is insufficient time for a jet to develop. If the spatial gradient of the LSW is taken into account for these bubbles, it does not appreciably affect any of the quantitative results shown, but does affect the shape behaviour. For example, for $\gamma \lesssim 1.5$, bubbles still collapse rapidly, but the spatial gradient induces a flat jet in the direction of LSW propagation, toward the wall, with a slightly higher centroid translation. Otherwise, the quantities of maximum volume, kinetic energy and Kelvin impulse are still negligible. For bubbles further away ($\gamma \gtrsim 1.5$), the spatial gradient appears to have no significant effect on either the shape dynamics or the main scalar quantities of interest. Regardless of the inclusion or exclusion of the spatial gradient in the far region, the bubble remains virtually spherical during passage of the RCW, and jet formation occurs only during the collapse phase, long after the LSW has passed, as in Case 1. The only quantity affected is the centroid translation (not shown), which is increased somewhat ($\sim$15–20 %) by the action of the spatial gradient.

4.5. *The role of vapour*

In our model, we have assumed the bubble contents to be comprised of a non-condensable gas (argon) plus water vapour. In addition, evaporation and condensation of vapour is modelled at the surface using the methods described by Szeri *et al.* (2003). To assess the effect of vapour on bubble dynamics, several simulations were performed without vapour inside the bubble and assuming no vapour transport at the bubble surface. Again, the initial conditions from Case 1 were assumed and only the STP portion of the LSW was used to drive the bubble. While the results are not shown here, our analysis indicates that the presence of vapour does not have an appreciable effect on the dynamics of the bubble: the quantities of maximum volume, kinetic energy, Kelvin impulse, and centroid translation are negligibly affected as well as their trends with respect to γ. There is one exception, however, for bubbles located relatively far from the boundary ($\gamma \gtrsim 3$), the kinetic energy at collapse is $\sim$20 % higher in the absence of vapour. For these cases, the bubble pressure is lower and the bubble collapses to a smaller volume, with a maximum jet velocity $\sim$15 % higher. Regardless, the maximum kinetic energy is unaffected by the presence or absence of vapour. Vapour tends to lower temperatures inside the bubble as water vapour dissociates at high temperatures (owing to rapid compression and adiabatic heating) and undergoes mainly endothermic reactions that lower the bulk temperature (Storey & Szeri 2000). Thus, when vapour is neglected, bubble temperatures are greater, but this is offset by the reduced number of moles inside the bubble (as vapour is not present to dissociate) and the pressure and minimum volume are reduced as a result. When vapour is included, the temperatures can be several times lower and the pressure several times greater than for the non-vapour case. Again, this only occurs for $\gamma \gtrsim 3$, but may have implications for the study of sonochemistry, for example.

As an aside, for bubbles that remain singly connected after the initial collapse, the presence of vapour inside the bubble has been shown to increase the amplitude and reduce the frequency of the afterbounces (Matula *et al.* 2002). This effect is not relevant to our study as we are interested only in the initial collapse during which jet impact causes the bubble to undergo a topological transition to a torus.

4.6. *Jet velocity and compressible effects*

Thus far, we have focused on the kinetic energy and Kelvin impulse, but jet velocity may also be an important factor in assessing substrate damage. The maximum jet velocity was calculated at each value of γ for all three cases, however, the results are not shown here. Unlike other quantities that have been considered, the maximum jet velocity in our simulations increases with larger standoff distance. Near the boundary, the onset of jet development occurs earlier in the collapse cycle, when the bubble wall velocity is relatively slow, resulting in lower jet speeds. Further from the boundary, the bubble shrinks to a smaller minimum volume and jets form later in the collapse when the bubble wall velocity is higher, allowing jets to achieve higher speeds. Figure 8 illustrates the decrease in minimum volume for increasing γ as well as the flattening of the bubble underside at small γ, which retards the jet motion. Our results indicate that for $\gamma \gtrsim 2.5$, the maximum Mach number exceeds 0.5, and for higher standoff distances can exceed 1.0. Although the limitations of our model preclude accurate calculations of jet velocity at Mach numbers approaching and exceeding 1.0, they are in line with other studies of shock–bubble interaction. For instance, Philipp *et al.* (1993) reported jet velocities about half the speed of sound for shock–bubble interaction near a plastic foil. Bourne & Field (1992) applied shocks to two-dimensional cavities in gelatin and observed jet velocities exceeding that of the incident shock. Also, Ding & Gracewski (1996) and Klaseboer *et al.* (2006) used different numerical methods to predict jet velocities greater than the speed of sound for bubbles interacting with shock waves in an infinite fluid.

Whereas the kinetic energy and Kelvin impulse may relate to damage caused by normal stresses at the substrate surface (Tomita & Shima 1986), high jet velocities can generate secondary shock waves that can induce damage as well (Bourne & Field 1995; Ohl 2002; Lindau & Lauterborn 2003). Therefore, in assessing stone comminution due to cavitation, the combined effect of these mechanisms must be considered. For a shock wave of given strength, the stresses induced on a nearby surface will diminish with increasing distance. Thus, while jet velocity increases with γ, the greatest damage incurred by secondary shock wave emission may occur for bubbles in the mid-range. In contrast, the kinetic energy and Kelvin impulse are greatest near the surface. Therefore, the influence of standoff distance on actual stone damage is not immediately clear. This analysis is supported by Bourne & Field (1995) who performed experiments on the asymmetric collapse of two-dimensional cavities in gelatin owing to interaction with plane shock waves. They demonstrated that for cavities near a rigid surface, the impact of jets was the primary contributor to damage, whereas for cavities positioned further away, the main contributor to surface damage was from the generation of secondary pressure waves that formed both at the moment of jet impact and during rebound of the cavity. Understanding the relative contributions to surface damage from both jet impact and secondary shock wave emission, and linking these to the bubble dynamics, is worthy of further study, but is beyond the scope of the present work.

Finally, we address the effects of compressibility that can become manifest for certain bubble collapses. In short, compressible effects are not expected to alter the qualitative trends with respect to γ shown here for the various quantities of interest. The main effect of compressibility is energy loss from the bubble through radiation of acoustic energy and shock waves. This predominantly occurs during the rebound of the bubble after it reaches minimum volume, and also at the point of jet impact in the case of a non-spherical collapse (Lindau & Lauterborn 2003; Sankin *et al.* 2005). Some energy will be reflected during the initial stage of shock–bubble interaction – owing to the large impedance mismatch between the gas and the liquid – and create an outward-propagating rarefaction wave. Ding & Gracewski (1996) simulated this phenomenon for a shock wave with a peak pressure of 20.5 MPa, but showed that the amplitude of the rarefaction wave is small relative to the imposed shock pressure, and its effect is localized to a small region surrounding the bubble. By comparison, the amplitude of the pressure wave emitted due to the rebound far exceeds that of the initial rarefaction wave. However, in the cases considered here, the jet impacts the opposite side of the bubble before minimum volume (rebound) is reached and the simulation is halted thereafter; thus, little energy is lost prior to this instant and is unlikely to affect the overall dynamics. It then follows that quantities such as kinetic energy at collapse, maximum Kelvin impulse, and centroid translation during the singly connected phase are not likely to be appreciably affected by compressibility. Determination of these quantities after transition to a toroidal geometry is not performed as the dissipative mechanisms of this process will tend to reduce the damage potential after jet impact (see § 2.5 for further discussion). In addition, as the fluid velocity is well below the speed of sound during the expansion phase, long after the LSW has passed, compressibility will have virtually no effect on maximum volume or the maximum kinetic energy (the latter of which occurs during the very early stages of expansion).

5. Conclusions

The results presented here allow us to draw several conclusions regarding the non-spherical collapse of bubbles excited by lithotripsy shock waves near a rigid surface. In the near region, the incident and reflected lithotripter waves interfere constructively, leading to enhanced bubble expansion and energetics of collapse as compared to the case when reflection is omitted. Further from the wall, destructive interference between the incident and reflected waves leads to a suppression of bubble dynamics.

This effect of the rigid surface on the bubble dynamics holds regardless of the initial bubble radius or its initial conditions (e.g. expanding, collapsing, or in equilibrium) at the time of impact with the LSW. The initial state of the bubble, however, does affect the magnitude of quantities such as kinetic energy and Kelvin impulse, but the presence of the wall still causes enhancement in the near region and suppression further away. In addition, the presence or absence of water vapour inside the bubble does not have an appreciable effect on the overall dynamics, but can dramatically alter the temperature and pressure in the bubble interior during collapse.

This work also yields several insights regarding the relationship between the LSW and the collapse process. First, the spatial gradient of the LSW has little effect on the bubble dynamics owing to both the small size of the bubble relative to the length of the LSW, and the quick passage of the LSW relative to the expansion time of the bubble. Thus, the non-spherical collapse is mediated by the asymmetry induced in the flow by the rigid boundary and not the spatial gradient of the LSW. It has also been shown that the STP is the main driver of the bubble dynamics, although the ITW can contribute as well. For bubbles located sufficiently far from the rigid boundary, the ITW can impart additional energy to the bubble – enough to overcome the compressive effect of the RCW – and lead to more vigourous collapses than those initiated by the STP alone. For bubbles located closer to the surface, the ITW has little effect and the subsequent RCW causes rapid collapse with little intensity. It was also demonstrated that the tail portion of the LSW significantly inhibits bubble expansion and collapse. The tail reduces the effect of constructive and destructive interference by the reflected wave, but by no means nullifies it.

In addition, we have shown that the maximum volume of the bubble is strongly correlated to the net work input by the LSW, regardless of the standoff distance and the presence or absence of reflection. Furthermore, the relationship between work input and maximum volume for non-spherical bubbles matches almost exactly that of a spherical bubble model by Iloreta *et al.* (2007). The relationship between work input and kinetic energy at collapse, for bubbles near the wall, is similarly direct. However, the dependence of Kelvin impulse on the work input is more subtle as it is mediated by the standoff distance and the form of the LSW input.

This work was supported by a grant from the US National Science Foundation Program in Biomedical Engineering and Research to Aid Persons with Disabilities. The authors are deeply grateful to Professor John Blake for his advice, Professor Pei Zhong for his interest and suggestions, and to Professor Edgar Knobloch for reviewing an early draft of this study.

REFERENCES

Best, J. P. 1993 The formation of toroidal bubbles upon the collapse of transient cavities. *J. Fluid Mech.* **251**, 79–107.

Best, J. P. & Kucera, A. 1992 A numerical investigation of non-spherical rebounding bubbles. *J. Fluid Mech.* **245**, 137–154.

Blake, J. R. & Gibson, D. C. 1987 Cavitation bubbles near boundaries. *Annu. Rev. Fluid Mech.* **19**, 99–123.

Blake, J. R., Taib, B. B. & Doherty, G. 1986 Transient cavities near boundaries. Part 1. Rigid boundary. *J. Fluid Mech.* **170**, 479–497.

Bourne, N. K. & Field, J. E. 1992 Shock-induced collapse of single cavities in liquids. *J. Fluid Mech.* **244**, 225–240.

Bourne, N. K. & Field, J. E. 1995 A high-speed photographic study of cavitation damage. *J. Appl. Phys.* **78**, 4423–4427.

Bourne, N. K. & Field, J. E. 1999 Shock-induced collapse and luminescence by cavities. *Phil. Trans. R. Soc. Lond.* A **357**, 295–311.

Calvisi, M. L. 2006 Shape stability and violent collapse of microbubbles interacting with acoustic waves and shocks. PhD dissertation, University of California, Berkeley.

Calvisi, M. L., Lindau, O., Blake, J. R. & Szeri, A. J. 2007 Shape stability and violent collapse of microbubbles in acoustic traveling waves. *Phys. Fluids* **19**, 047101.

Church, C. C. 1989 A theoretical study of cavitation generated by an extracorporeal shock wave lithotripter. *J. Acoust. Soc. Am.* **86**, 215–227.

Crum, L. A. 1979 Surface oscillations and jet development in pulsating bubbles. *J. Phys. Paris* **41**, 285–288.

Ding, Z. & Gracewski, S. M. 1996 The behaviour of a gas cavity impacted by a weak or strong shock wave. *J. Fluid Mech.* **309**, 183–209.

Hamilton, M. F., Ilinskii, Y. A., Meegan, G. D. & Zabolotskaya, E. A. 2005 Interaction of bubbles in a cluster near a rigid surface. *Acoust. Res. Lett. Online* **6**, 207–213.

Iloreta, J. I., Zhou, Y., Sankin, G. N., Zhong, P. & Szeri, A. J. 2007 Assessment of shock wave lithotripters via cavitation potential. *Phys. Fluids* **19**, 086103.

Iloreta, J. I., Fung, N. & Szeri, A. J. 2008 Dynamics of bubbles near a rigid surface subjected to a lithotripter shock wave. Part 1. Consequences of interference between incident and reflected waves. *J. Fluid Mech.* **616**, 43–61.

Klaseboer, E., Turangan, C., Fong, S. W., Liu, T. G., Hung, K. C. & Khoo, B. C. 2006 Simulations of pressure pulse-bubble interaction using boundary element method. *Comput. Meth. Appl. Mech. Engng.* **195**, 4287–4302.

Klaseboer, E., Fong, S. W., Turangan, C. K., Khoo, B. C., Szeri, A. J., Calvisi, M. L., Sankin, G. N. & Zhong, P. 2007 Interaction of lithotripter shockwaves with single inertial cavitation bubbles. *J. Fluid Mech.* **593**, 33–56.

Kodama, T. & Tomita, Y. 2000 Cavitation bubble behavior and bubble–shock wave interaction near a gelatin surface as a study of *in vivo* bubble dynamics. *Appl. Phys.* B *Lasers Optics* **70**, 139–149.

Lindau, O. & Lauterborn, W. 2003 Cinematographic observation of the collpase and rebound of a laser-produced cavitation bubble near a wall. *J. Fluid Mech.* **479**, 327–348.

Matula, T. J., Hilmo, P. R., Storey, B. D. & Szeri, A. J. 2002 Radial response of individual bubbles subjected to shock wave lithotripsy pulses *in vitro*. *Phys. Fluids* **14**, 913–921.

Ohl, C. D. 2002 Cavitation inception following shock wave passage. *Phys. Fluids* **14**, 3512–3521.

Ohl, C. D. & Ikink, R. 2003 Shock-wave induced jetting of micron-sized bubbles. *Phys. Rev. Lett.* **90**, 214502.

Pearson, A., Blake, J. R. & Otto, S. R. 2004 Jets in bubbles. *J. Engng Maths.* **48**, 391–412.

Philipp, A., Delius, M., Scheffczyk, C., Vogel, A. & Lauterborn, W. 1993 Interaction of lithotripter-generated shock waves with air bubbles. *J. Acoust. Soc. Am.* **93**, 2496–2509.

Pishchalnikov, Y. A., Sapozhnikov, O. A., Bailey, M. R., Williams, J. C., Cleveland, R. O., Colonius, T., Crum, L. A., Evan, A. P. & McAteer, J. A. 2003 Cavitation bubble cluster activity in the breakage of kidney stones by lithotripter shockwaves. *J. Endourol.* **17**, 435–446.

Pishchalnikov, Y. A., McAteer, J. A., Williams, J. C., Pishchalnikova, I. V. & Vonderhaar, R. J. 2006 Why stones break better at slow shockwave rates than at fast rates: *in vitro* study with a research electrohydraulic lithotripter. *J. Endourol.* **20**, 537–541.

Prosperetti, A. & Lezzi A. 1986 Bubble dynamics in a compressible liquid. Part 1. First-order theory. *J. Fluid Mech.* **168**, 457–478.

Sankin, G. N. & Zhong, P. 2006 Interaction between shock wave and single inertial bubbles near an elastic boundary. *Phys. Rev.* E **74**, 046304.

Sankin, G. N., Simmons, W. N., Zhu, S. L. & Zhong, P. 2005 Shock wave interaction with laser-generated single bubbles. *Phys. Rev. Lett.* **95**, 034501.

Sato, K., Tomita, Y. & Shima, A. 1994 Numerical analysis of a gas bubble near a rigid boundary in an oscillatory pressure field. *J. Acoust. Soc. Am.* **95**, 2416–2424.

Storey, B. D. & Szeri, A. J. 2000 Water vapour, sonoluminescence and sonochemistry. *Proc. R. Soc. Lond.* A **456**, 1685–1709.

Szeri, A. J., Storey, B. D., Pearson, A. & Blake, J. R. 2003 Heat and mass transfer during the violent collapse of non-spherical bubbles. *Phys. Fluids* **15**, 2576–2586.

Taib, B. B. 1985 Boundary integral method applied to cavitation bubble dynamics. PhD dissertation, University of Wollongong.

Tomita, Y. & Shima, A. 1986 Mechanisms of impulsive pressure generation and damage pit formation by bubble collapse. *J. Fluid Mech.* **169**, 535–564.

Zabolotskaya, E. A., Ilinskii, Y. A., Meegan, G. D. & Hamilton, M. F. 2004 Bubble interactions in clouds produced during shock wave lithotripsy. *Proc. IEEE Ultrasonics Symp.*, pp. 890–893.